Contrast Media & Molecular Imaging

Emergent Techniques for Transporter and Receptor-Based Imaging and Interventional Molecular Imaging

Lead Guest Editor: Paulo H. Rosado-De-Castro
Guest Editors: David Yang, Hwan-Jeong Jeong, Kazuma Ogawa, Marcos F. H. Dos Santos, and Skye Yeh

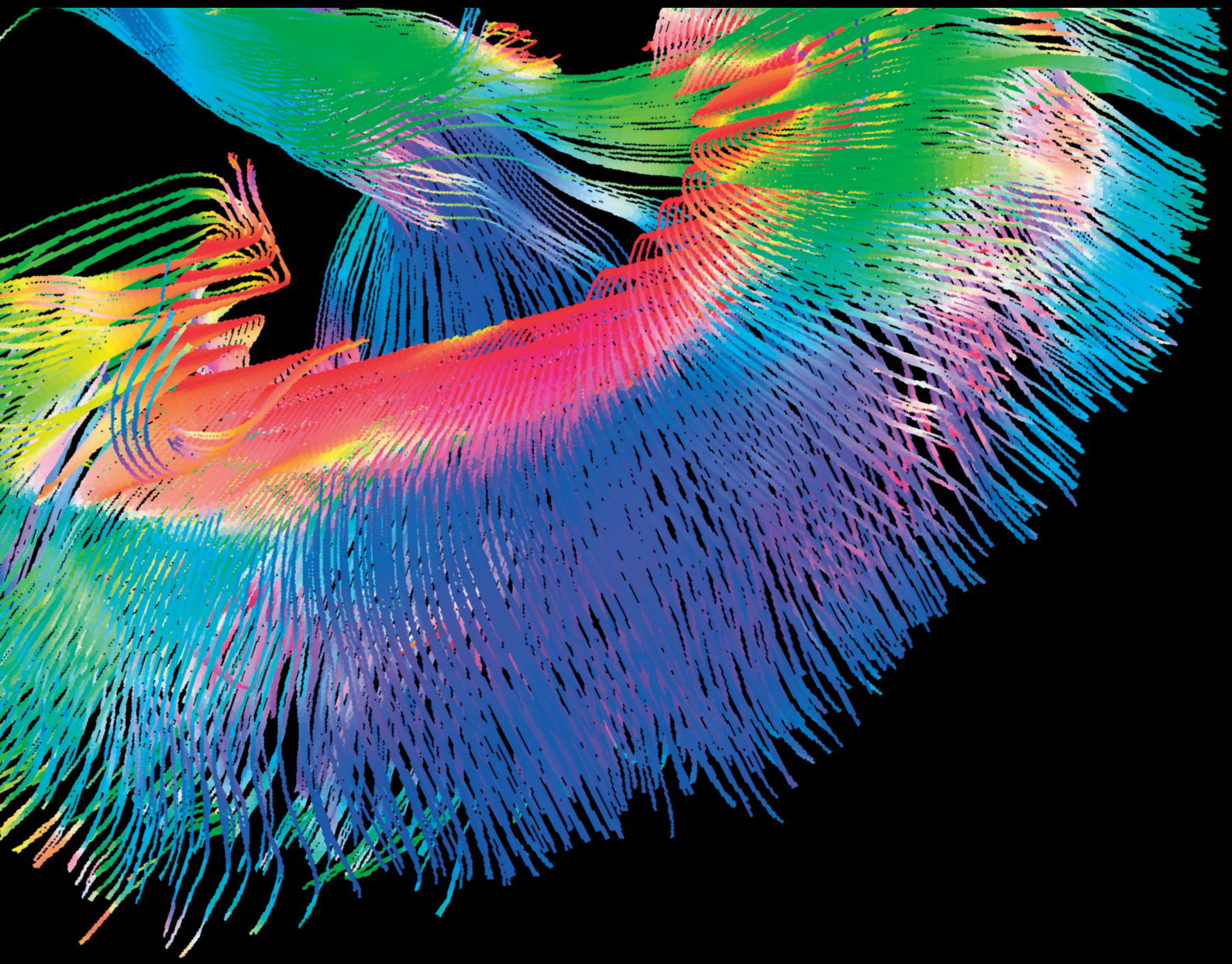

Emergent Techniques for Transporter and Receptor-Based Imaging and Interventional Molecular Imaging

Contrast Media & Molecular Imaging

Emergent Techniques for Transporter and Receptor-Based Imaging and Interventional Molecular Imaging

Lead Guest Editor: Paulo H. Rosado-De-Castro
Guest Editors: David Yang, Hwan-Jeong Jeong, Kazuma Ogawa, Marcos F. H. Dos Santos, and Skye Yeh

Editorial Board

Contents

Hindawi
Contrast Media & Molecular Imaging
Volume 2018, Article ID 7615308, 2 pages
https://doi.org/10.1155/2018/7615308

Editorial

Emergent Techniques for Transporter and Receptor-Based Imaging and Interventional Molecular Imaging

Paulo Henrique Rosado-De-Castro,[1,2,3] **David Yang**,[4] **Hwan-Jeong Jeong**,[5,6] **Kazuma Ogawa**,[7] **Marcos Fabio Henriques DosSantos**,[1,2] **and Skye Hsin-Hsien Yeh**[8]

[1]*Institute of Biomedical Sciences, Federal University of Rio de Janeiro, 21941-590 Rio de Janeiro, RJ, Brazil*
[2]*Department of Radiology, Federal University of Rio de Janeiro, 21941-913 Rio de Janeiro, RJ, Brazil*
[3]*D'Or Institute for Research and Education, 22281-100 Rio de Janeiro, RJ, Brazil*
[4]*Vyripharm Biopharmaceuticals, 77021 Houston, Texas, USA*
[5]*Department of Nuclear Medicine, Molecular Imaging and Therapeutic Medicine Research Center, Chonbuk National University Medical School and Hospital, Jeonju, Jeollabuk-do 54896, Republic of Korea*
[6]*Research Institute of Clinical Medicine, Biomedical Research Institute, Chonbuk National University Hospital, Chonbuk National University, Jeonju, Jeollabuk-do 54896, Republic of Korea*
[7]*Institute for Frontier Science Initiative, Kanazawa University, Kakuma-machi, Kanazawa, Ishikawa 920-1192, Japan*
[8]*Brain Research Center, National Yang-Ming University, 11221 Taipei, Taiwan*

Correspondence should be addressed to Paulo Henrique Rosado-De-Castro; paulo.rosado@idor.org

Received 19 September 2018; Accepted 19 September 2018; Published 20 December 2018

The growing field of molecular imaging has allowed non-invasive *in vivo* tracking of pharmacological and biological pathways. Translational studies have fast-tracked the application of observations from basic findings to the clinical setting. Amongst the most encouraging methods are transporter and receptor-based imaging, where probes permit the diagnosis of disorders, in addition to the prognostication and evaluation of response to treatments. Precise preoperative staging, surgical preparation, and intraoperative imaging can be achieved using tracers with high sensitivity and specificity. A total of 14 manuscripts were submitted to this special issue, and after rigorous review, 4 were accepted, including one preclinical and three clinical studies.

J. H. Choi et al. created a new approach of radiochemical production via photoactivated reaction to make ^{18}F-labeled PET tracers using small molecular and RGD peptides, which can specifically and strongly bind to integrin $\alpha v\beta 3$. Integrin $\alpha v\beta 3$ is related to angiogenic endothelial and different tumors, including breast, prostate, lung, and ovarian cancers. *In vivo* PET imaging after intravenous administration of an ^{18}F-labeled compound to RR1022 sarcoma-bearing Sprague Dawley rats demonstrated a high tumor-to-background ratio, indicating it can be useful for evaluation of tumor angiogenic response.

D. Dai et al. carried out a Phase 2 trial designed to evaluate whether technetium-99m-labeled ethylenedicysteine-glucosamine (^{99m}Tc-EC-G) SPECT/CT was noninferior to ^{18}F-labeled fludeoxyglucose (^{18}F-FDG) PET/CT in 17 patients with confirmed nonsmall cell lung cancer (NSCLC). The authors found 100% concordance between both tracers for primary tumor detection and 70% agreement for metastatic tumor detection, indicating that ^{99m}Tc-EC-G SPECT/CT may be a clinically useful radiotracer, warranting the preparation of Phase 3 study.

Y. J. Jeong et al. analyzed dopamine transporters (DATs) with ^{18}F-labeled 3-b-(4-iodophenyl)nortropane (FP-CIT) PET on patients with Parkinsonism, cerebellar, and autonomic characteristics in multiple system atrophy with cerebellar ataxia (MSA-C). A total of 49 subjects clinically diagnosed with possible or probable MSA-C were included. The authors found statistically significant differences in postural instability, rigidity, asymmetry, bradykinesia, and specific uptake ratio (SUR) between groups. A subgroup of

22 subjects received dopaminergic medications. Interestingly, all seven subjects with normal exams presented no modification, whereas 10 out of 15 subjects with abnormal exams presented clinical progress.

Finally, D. Dai et al. compared 3D positron emission mammography (PEM) with whole-body PET (WBPET) for patients with breast cancer. A total of 410 women with normal breast, benign tumors, or highly suspicious malignant lesions were randomized at 1 : 1 ratio for imaging with WBPET followed by 3D-PEM or 3D-PEM followed by WBPET. Lumpectomy or mastectomy was carried out on eligible subjects after imaging. The authors reported that 3D-PEM had sensitivity and specificity of 92.8% and 54.5%, respectively, while WBPET had sensitivity and specificity of 95.7% and 56.8%, respectively.

In conclusion, significant developments have been achieved in transporter and receptor-based molecular imaging, and the original articles in this special issue underscore progresses for translation of these promising techniques into the clinic.

Paulo Henrique Rosado-De-Castro
David Yang
Hwan-Jeong Jeong
Kazuma Ogawa
Marcos Fabio Henriques DosSantos
Skye Hsin-Hsien Yeh

Conflicts of Interest

The authors declare that they have no conflicts of interest.

Hindawi
Contrast Media & Molecular Imaging
Volume 2018, Article ID 4617493, 10 pages
https://doi.org/10.1155/2018/4617493

Research Article

Light-Triggered Radiochemical Synthesis: A Novel ^{18}F-Labelling Strategy Using Photoinducible Click Reaction to Prepare PET Imaging Probes

Ji Hae Choi,[1,2] Doori Oh,[1,2] In Sun Kim,[1,2] Hyeon-Soo Kim,[1,2] Minjoo Kim,[1,2] Eun-Mi Kim,[1,2] Seok Tae Lim,[1,2] Myung-Hee Sohn,[1,2] Dong Hyun Kim,[1,2,3] and Hwan-Jeong Jeong[1,2]

[1]*Department of Nuclear Medicine, Molecular Imaging and Therapeutic Medicine Research Center, Chonbuk National University Medical School and Hospital, Jeonju, Jeollabuk-do 54896, Republic of Korea*
[2]*Research Institute of Clinical Medicine, Biomedical Research Institute, Chonbuk National University Hospital, Chonbuk National University, Jeonju, Jeollabuk-do 54896, Republic of Korea*
[3]*Kaibiotech, 20 Geonji-ro, Deokjin-gu, Jeonju, Jeollabuk-do 54896, Republic of Korea*

Correspondence should be addressed to Dong Hyun Kim; dhdh.kim@gmail.com and Hwan-Jeong Jeong; jayjeong@jbnu.ac.kr

Received 10 November 2017; Revised 25 April 2018; Accepted 7 May 2018; Published 25 June 2018

Academic Editor: Giancarlo Pascali

Novel probe development for positron emission tomography (PET) is leading to expanding the scope of molecular imaging. To begin responding to challenges, several biomaterials such as natural products and small molecules, peptides, engineered proteins including affibodies, and antibodies have been used in the development of targeted molecular imaging probes. To prepare radiotracers, a few bioactive materials are unique challenges to radiolabelling because of their complex structure, poor stability, poor solubility in aqueous or chemical organic solutions, and sensitivity to temperature and nonphysiological pH. To overcome these challenges, we developed a new radiolabelling strategy based on photoactivated 1,3-dipolar cycloaddition between alkene dipolarophile and tetrazole moiety containing compounds. Herein, we describe a light-triggered radiochemical synthesis via photoactivated click reaction to prepare ^{18}F-radiolabelled PET tracers using small molecular and RGD peptide.

1. Introduction

Molecular imaging probes provide better understanding of fundamental pathways to monitor biochemical changes *in vivo*. They are important for diagnosis, monitoring of therapeutic response, and drug development [1, 2]. PET is an attractive nuclear medicine technique that serves as a noninvasive and functional imaging modality at picomolar levels *in vivo* with excellent sensitivity based on positron-emitting radionuclide [3, 4]. PET scan information can be used to assess biological processes *in vivo* during early stages of various diseases, including cancer, heart disease, and dementia in Alzheimer's disease and Parkinson's disease. It is also important to assess response to chemotherapy or radiotherapy in various malignancies [5, 6]. Several radiopharmaceuticals targeting specific diseases have been developed. Among various PET tracers, FDG (2-deoxy-2-[^{18}F]fluoro-D-glucose) is the most commonly used one in nuclear medicine and molecular cellular biology. FDG was discovered approximately 40 years ago [7]. It has led to a new medical paradigm involving more accurate diagnosis via functional information through quantitative analysis in fields of oncology, neuroscience, and cardiology. Several studies on ^{18}F-radiolabelled targeting radiotracers for disease monitoring via PET images have been reported. Fluorine-18 has a relatively long half-life ($T_{1/2} = 109.8$ min) and low energy (0.635 MeV) that permits PET imaging protocols with a duration up to 6 h and short positron linear range in tissue due to low positron energy, resulting in high sensitivity in PET imaging [8, 9]. However, ^{18}F-incorporation into biotargeting vectors can be challenging because it must be performed rapidly and efficiently under mild radiolabelling conditions due to short

half-life of the radioisotope and regioselectivity labelling of high specificity with acceptable radiochemical yield [10]. To overcome these obstacles, ^{18}F-radiolabelling strategies using ^{18}F-prosthetic groups such as *N*-succinimidyl-4-[^{18}F]fluorobenzoate ([^{18}F]SFB) [11–15], 2-bromo-*N*-[3-(2-[^{18}F]fluoropyridin-3-yloxy)propyl]acetamide ([^{18}F]FPyBrA) [16, 17], and *N*-(4-[^{18}F]fluorobenzyl)-2-bromoacetamide ([^{18}F]FBBA) [18, 19] have been introduced for labelling of amine and sulfhydryl functionalities of sensitive biomolecules, including small molecules, peptides, and proteins. Click chemistry, copper (I)-catalyzed Huisgen 1,3-dipolar cycloaddition, is still one of the attractive approaches to prepare targeted molecular imaging probes for PET by radiolabelling with small molecules, peptides, and proteins. A number of novel radiotracers have been reported through the click chemistry, including copper-free approaches to avoid toxicity to humans who are susceptible to even low levels of copper [20–27]. Recently, Lin and coworkers have reported that advanced photoinducible 1,3-dipolar cycloaddition reactions show extremely rapid reaction rate and high regioselectivity of desired product without opposite regioisomer under photoactivated mild condition [28–30]. This has stimulated efforts to further develop ^{18}F-radiolabelling strategy to create a new labelling platform using photoactivation by UV radiation. Herein, we report a new strategy that utilizes photoactivated click chemistry between ^{18}F-labelled terminal alkene dipolarophile and tetrazole moiety compound under radiation using UV light source for a biocompatible and mild reaction with significantly high radiochemical yield and molar activity of desired radiolabelled product for PET imaging.

2. Results and Discussion

First, to determine whether photoinducible click reaction with radiolabelled compound could be used as a novel approach to prepare radiopharmaceuticals, we examined photoactivated radiolabelling between ^{18}F-radiolabelled compound [^{18}F]**2** and 2,5-diaryl tetrazole compound **3** under mild condition using handheld 302 nm UV lamp. For feasibility study of radiochemical synthesis using photoinducible reaction, we chose a 2-(allyloxy)ethanol as a terminal alkene moiety. It is commercially available. It readily undergoes a catalyst-free cycloaddition reaction with photoinduced nitrile imine from tetrazole compound. To prepare ^{18}F-radiolabelled compound [^{18}F]**2**, trimethylammonium triflate precursor **1** was prepared from 4-(dimethylamino)benzoyl chloride and conjugated with 2-(allyloxy)ethanol followed by conversion of the dimethylamino functional group using methyl triflate at room temperature. Synthesis of 2,5-diaryl tetrazole compound **3** was performed using a previously reported procedure [11]. Radiolabelling of precursor **1** was carried out with K[^{18}F]F in CH_3CN (prepared following azeotropic distillation of a CH_3CN solution containing K_2CO_3 and Kryptofix 2.2.2) at 90°C for 10 min to give 2-(allyloxy)ethyl-4-[^{18}F]fluorobenzoate [^{18}F]**2** followed by photoinduced cycloaddition with 2,5-diaryl tetrazole compound **3** in situ (Scheme 1) at room temperature under 302 nm UV radiation for 30 min. The resulting radiolabelled compound [^{18}F]**2** was obtained with 80% yield as determined by radio-TLC. It was used without purification for subsequent photoinducible click reaction with tetrazole compound **3**. Photo click reaction between ^{18}F-radiolabelled terminal alkene compound [^{18}F]**2** and tetrazole compound **3** produced the desired product [^{18}F]**4**. It was isolated by semipreparative HPLC with an overall yield of 20–27% (decay-corrected, $n = 4$). It had high molar activity of 30–112 GBq/μmol ($n = 4$) with radiochemical purity >98%. Purified [^{18}F]**4** was identified with nonradioactive reference compound **4** by analytical HPLC (Figure 1). Increasing irradiation time to 5–30 min of 302 nm UV lamp resulted in the maximum radiochemical yield at room temperature. In order to investigate the radiochemical yield with reaction time, the best result was obtained at 30 min under the same reaction condition with the time difference of 5 to 30 min. Heating conditions were not considered for the application of temperature-sensitive proteins or peptides. Results indicated that the radiochemical synthesis through photoinducible reaction could be performed under mild conditions, which was possible for both large and small molecules. To evaluate the wavelength effect of light source, we carried out optimized experiment with tetrazole compound **3** and [^{18}F]**2** under irradiation of different light sources such as halogen and red LED (720 nm) at room temperature. The desired product [^{18}F]**4** was obtained when 302 nm UV light was employed. However, no reaction was observed when halogen or red LED was employed (Figure 2). Of various light sources, only 302 nm UV led to a good conversion to intermediate nitrile imine when 2,5-diaryl tetrazole compound **3** was used. These results demonstrated that photoactivated click reaction between 2-(allyloxy)ethyl-4-[^{18}F]fluorobenzoate [^{18}F]**2** and nitrile imine was efficient under irradiation with 302 nm UV. Of various factors investigated for photoactivated click reaction, UV wavelength was found to be the most important factor to synthesize the desired product. We aimed to develop water-soluble mass materials such as peptides or proteins as imaging agents. Hence, we subsequently applied the method to radiolabel cyclic RGD peptide and evaluated tumor targeting ability of integrin $\alpha_v\beta_3$ as a molecular imaging probe. Integrin $\alpha_v\beta_3$ is associated with angiogenic endothelial as well as tumor cells, including cancers of the prostate, skin, ovary, kidney, lung, and breast. RGD peptides can specifically and strongly bind to integrin $\alpha_v\beta_3$ [31, 32]. Cyclic RGDyK peptide was selected as targeting material due to its high binding affinity to tumor cells, small size peptide, and available description in the literature on tumor studies. We performed conjugation with 2,5-diaryl tetrazole benzoic acid (**5**) to form 2,5-diaryl tetrazole-RGD (**7**) by reaction of NH_2-Lys-RGD with *N*-hydroxysuccinimide active ester of 2,5-diaryl tetrazole (Scheme 2). It was purified with HPLC. For radiochemical synthesis of the desired ^{18}F-labelled RGD peptide ([^{18}F]**8**), photoactivated click reaction was performed between 2,5-diaryl tetrazole-RGD peptide (**7**) and 2-(allyloxy)ethyl-4-[^{18}F]fluorobenzoate ([^{18}F]**4**) using 302 nm UV lamp for irradiation at room temperature. After 20 min of reaction, the crude mixture was purified with HPLC.

Identity of the radiolabelled product ([^{18}F]**8**) was confirmed by HPLC retention time after coinjection with authentic nonradioactive compound **8**. Radiochemical synthesis of [^{18}F]**8** was successfully carried out by photoactivation. Radiochemical yield from [^{18}F]fluoride was 10–12% ($n = 4$) by two-step one-pot reaction. The desired product showed excellent purity with

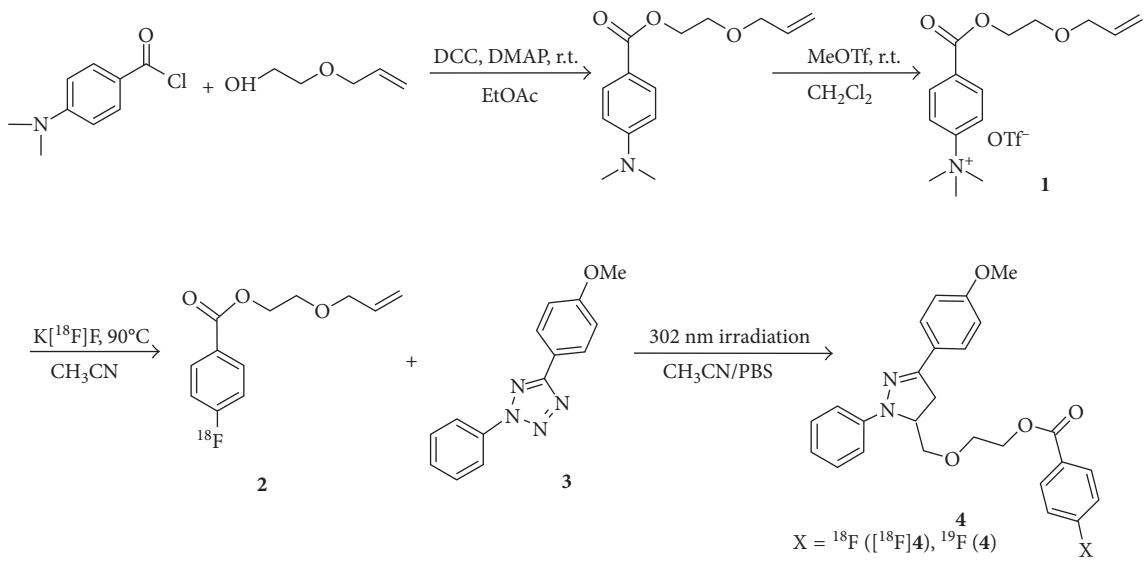

Scheme 1: Synthesis of [^{18}F]**4** and **4** using photoinducible click reaction.

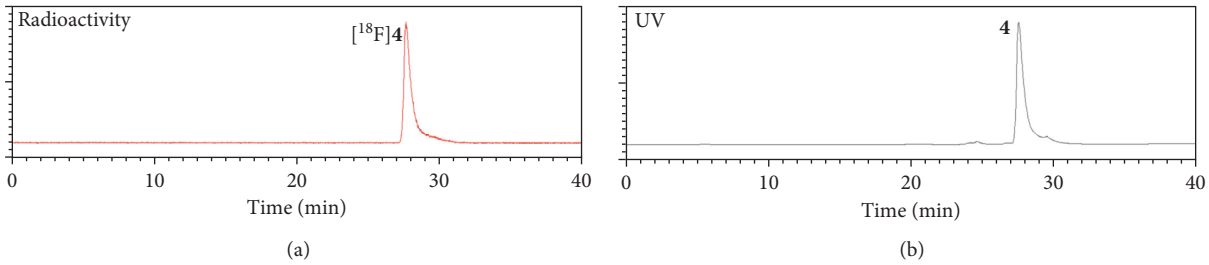

Figure 1: Analytic HPLC profile of [^{18}F]**4** (a) with coinjection of the authentic compound **4** (b).

adequate molar activities (20–72 GBq/μmol) in a total synthesis time of 95 min (including HPLC purification and reformulation). Based on these results, introducing a 2-(allyloxy)ethyl-4-[^{18}F]fluorobenzoate ([^{18}F]**2**) tag into peptide is suitable and effective due to the use of aqueous reaction media at room temperature and high chemoselectivity without requiring toxic metal catalyst. Biologically, the uptake of [^{18}F]**8** by U87MG tumor cell was increased in a time-dependent manner, plateauing between 60 and 120 min. Furthermore, U87MG cell blocking study using nonradiolabelled c(RGDyK) peptide showed cell uptake inhibition indicative of specific binding of [^{18}F]**8** to integrin $\alpha_v\beta_3$ expressed in U87MG glioblastoma cells (Figure 3).

In vivo PET imaging following intravenous injection of [^{18}F]**8** (4.66 MBq tail-vein injected) to RR1022 tumor-bearing SD rats showed tumor uptake of [^{18}F]**8** with renal clearance of ^{18}F-activity and high tumor-to-background contrast (tumor/muscle = 53.5 and 76.2 at 1 h and 2 h, resp.). No significant defluorination from [^{18}F]**8** uptake at bone was observed up to 2 h after injection. Furthermore, inhibition study showed that the excess amount (10 mg/kg) of c(RGDyK) peptide significantly blocked [^{18}F]**8** uptake in the tumor (tumor/muscle = 8.2 and 6.3 at 1 h and 2 h, resp.) (Figure 4). These *in vivo* imaging studies indicated that ^{18}F-labelled RGD peptide via photoinduced 1,3-dipolar cycloaddition could successfully visualize tumor *in vivo* through integrin $\alpha_v\beta_3$.

3. Conclusion

Our results suggest that ^{18}F-labelled RGD([^{18}F]**8**) radiotracer is useful for monitoring tumor response in angiogenesis research. The development of novel radiolabelling method for diagnosis of various diseases including cancer has benefit for mild conditions as an important approach to obtain accurate imaging. Photoinduced 1,3-dipolar cycloaddition using ^{18}F-radioisotope is an efficient radiolabelling strategy to prepare molecular imaging probes. It could be applied as a bio-orthogonal approach for chemical modification in biomedical research. Further study is required on the application of such photoinducible radiolabelling strategy based on its high availability and excellent chemoselectivity.

4. Materials and Methods

Benzenesulfonyl hydrazide, sodium nitrite, aniline, 4-fluorobenzoic acid, *N*,*N*′-dicyclohexylcarbodiimide (DCC), 4-dimethylaminopyridine (DMAP), 2-allyloxyethanol, dimethylaminobenzoyl chloride, methyl trifluoromethanesulfonate (MeOTf), triethylamine (TEA), *N*-hydroxysuccinimide, 1-ethyl-3-3-dimethylaminopropylcarbodiimide (EDC), 4-formylbenzoic acid, and DIPEA (*N*,*N*′-diisopropylethylamine) of ACS grade were purchased from Sigma-Aldrich

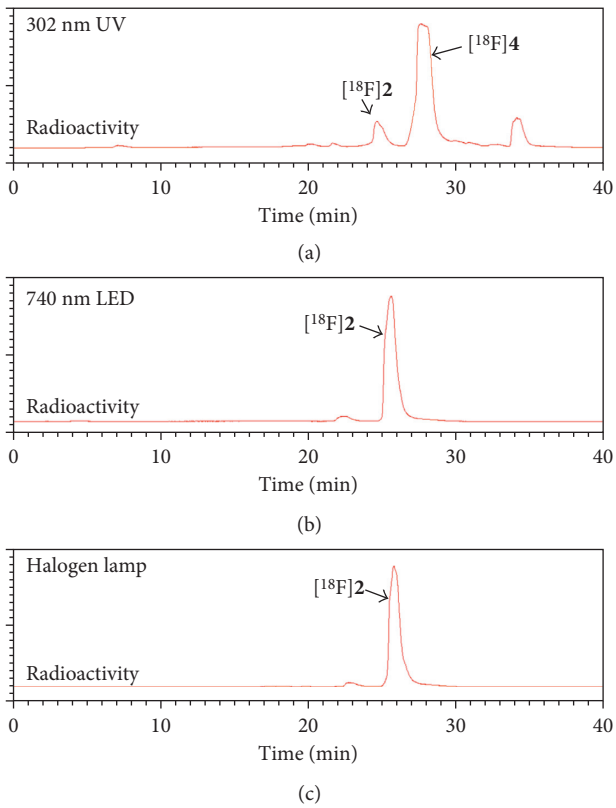

Figure 2: Comparison of light effect for photoinducible click reaction. (a) 302 nm UV lamp, (b) 740 nm LED, and (c) halogen lamp. The desired photoinduced radiolabelled compound [^{18}F]**4** was obtained only under irradiation of 302 nm UV (a).

(St. Louis, MO, USA). c(RGDyK) was purchased from Futurechem (Seoul, Korea). All chemicals were used without further purification unless otherwise noted. [^{18}F]Fluoride ion was produced from cyclotron (KIRAMS, South Korea) with 13 MeV proton irradiation. Flash column chromatography was performed using 230–400 mesh silica gel (Merck KGaA, Darmstadt, Germany). Radio-TLC was analyzed using a System 200 Imaging Scanner (BioScan, CA, USA). Purification was performed with a spectra system SCM100 degasser, a P4000 pump, and a UV-Vis 3000 detector (Thermo Scientific, Waltham, MA, USA). Absorbance was monitored at 214 nm with a C18 reverse-phase HPLC column (250 mm × 10 mm, 5 μm, Thermo Scientific, MA, USA). ChromQuest 4.2 software was used to record chromatograms. NMR spectra were recorded with a 600 MHz FT-NMR (JNM-EAC600, JEOL, Tokyo, Japan). High-resolution mass spectra (m/z) were recorded with electron ionization (EI, DFS (Thermo Scientific, Germany)) and fast atom bombardment (FAB, JMS-700 (JEOL, Tokyo, Japan)) at KBSI (Seoul, Korea).

4.1. Synthesis of 2-(Allyloxy)ethyl 4-(dimethylmino)benzoate. 2-Allyloxyethanol (2.0 mL, 18.7 mmol) was added to 4-*N*,*N*-dimethylaminobenzoyl chloride (0.5 g, 2.72 mmol) and triethylamine (0.76 mL, 5.44 mmol) in 10 mL of dichloromethane in a flame-dried flask with nitrogen stream. The reaction mixture was stirred for two hours at room temperature. The reaction mixture was then diluted with 50 mL of ethyl acetate and 30 ml of water. The product of organic layer was washed twice with 30 mL of water, and the organic layer was washed with 50 mL of brine. The organic layer was dried over sodium sulfate, evaporated, and purified with flash column chromatography (ethyl acetate : hexane = 1 : 5) to obtain a yellow oil product with yield of 55% (373.7 mg). ^{1}H NMR (600 MHz, $CDCl_3$) data were δ (ppm) = 7.91 (m, 2H), 6.63 (m, 2H), 5.90 (m, 1H), 5.29 (m, 1H), 5.18 (m, 1H), 4.40 (m, 2H), 4.05 (m, 2H), 3.74 (m, 2H), and 3.01 (s, 6H). ^{13}C NMR (150 MHz, $CDCl_3$) data were δ (ppm) = 167.00, 153.39, 134.68, 131.48, 117.29, 116.95, 110.75, 72.22, 68.37, 63.57, and 40.14. FAB MS calculated for $C_{14}H_{19}O_3N_1Na_1$ was 272.1257 m/z [M + Na]. It was also found to be 272.1257.

*4.2. Synthesis of 4-((2-(Allyloxy)ethoxy)carbonyl)-N,N,N-trimethylbenzenaminium (**1**).* To a solution of 2-(allyloxy) ethyl 4-(dimethylamino)benzoate (0.3 g, 1.20 mmol) dissolved in 2 mL of dichloromethane, methyl trifluoromethanesulfonate (0.27 mL, 2.40 mmol) was added. The mixture was stirred for two hours with nitrogen stream at room temperature. The reaction mixture was evaporated, and the resulting crude mixture was dissolved in 0.5 mL of ethanol. The product was crystallized with 100 mL of diethyl ether and dried to obtain a compound with a yield of 38% (122 mg). ^{1}H NMR (600 MHz, $CDCl_3$) data were δ (ppm) = 8.26 (d, J = 8.4 Hz, 2H), 7.92 (d, J = 9 Hz, 2H), 5.94–5.88 (m, 1H), 5.29 (d, J = 17.1 Hz, 1H), 5.20 (d, J = 10.5, 1H), 4.51 (t, J = 9.6 Hz, 2H), 4.06 (t, J = 2.4 Hz, 1H),

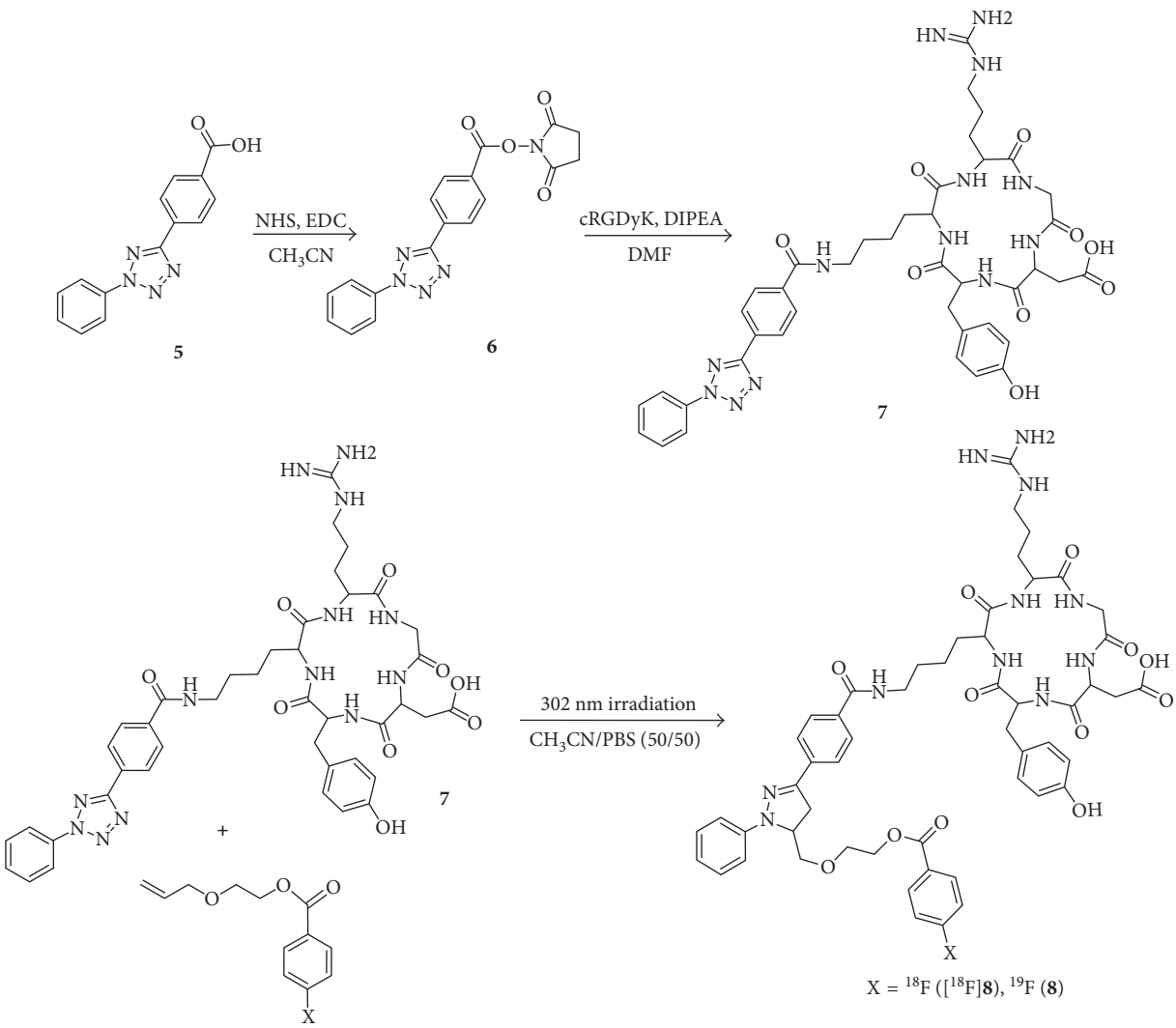

Scheme 2: Synthesis of ^{18}FB-PEGhc-RGD ([^{18}F]**8**) and **8** using photoinducible click reaction.

4.05 (t, $J = 2.4$ Hz, 1H), and 3.78 (s, 9H). ^{13}C NMR (150 MHz, $CDCl_3$) data were δ (ppm) = 164.65, 150.42, 134.50, 132.13, 131.34, 120.50, 116.09, 71.64, 67.67, 64.58, and 56.39. FAB MS calculated for $C_{15}H_{22}O_3N_1$ was 264.1594 m/z [M]. It was found to be 264.1594.

*4.3. Synthesis of 2-(Allyloxy)ethyl 4-[^{18}F]fluorobenzoate ([^{18}F]**2**).* Aqueous [^{18}F]fluoride of 0.76 GBq was added to an open glass reaction vessel containing 1 mL of Kryptofix 2.2.2 of solution (5 mg of Kryptofix 2.2.2 in 800 μL of acetonitrile and 1.5 mg of K_2CO_3 in 200 μL of H_2O). Azeotropic distillation was carried out to remove water at 95°C with a nitrogen stream. This procedure was repeated 4-5 times by further addition of 20 μL anhydrous acetonitrile until a white powder was obtained. The resulting K[^{18}F]F complex was dissolved in acetonitrile (200 μL). The resulting K[^{18}F]F solution was transferred to a reaction vial containing 4-((2-(allyloxy)ethoxy)carbonyl)-*N*,*N*,*N*-trimethylbenzenaminium (2 mg) and heated at 100°C with stirring for 20 min. At the end of the reaction, ^{18}F-labelled desired compound showed a yield of 79% on radio-TLC using 1 : 5 mixture of ethyl acetate-hexane as developing solvent. We used crude mixture of [^{18}F]**2** in the next step for photoinducible click reaction without purification.

*4.4. Synthesis of 2-(Allyloxy)ethyl 4-Fluorobenzoate (**2**).* Synthesis of 2-(allyloxy)ethyl 4-fluorobenzoate was carried out according to the published method of Vaidyanathan et al. [33] with slight modifications. Briefly, 2-allyloxyethanol (0.76 ml, 0.71 mmol) was added to a mixture of 4-fluorobenzoic acid (0.1 g, 0.71 mmol), DCC (0.15 g, 0.71 mmol), and DMAP (0.6 mg, 8.0 mmol) in 4 mL of ethyl acetate with a N_2 stream in a flask dried with a heat gun. The reaction mixture was stirred at room temperature overnight, and a white precipitate was filtrated out. After removing the precipitate, the residual reaction mixture was evaporated and purified by flash column chromatography (ethyl acetate : hexane = 1 : 5), resulting in a colorless oil with a yield of 42% (67.6 mg). 1H NMR (600 MHz, $CDCl_3$) data were δ (ppm) = 8.10 (m, 2H), 7.13 (t, $J = 8.6$ Hz, 2H), 5.96 (m, 1H), 5.33 (dd, $J = 38.6$ Hz, 16.8 Hz,

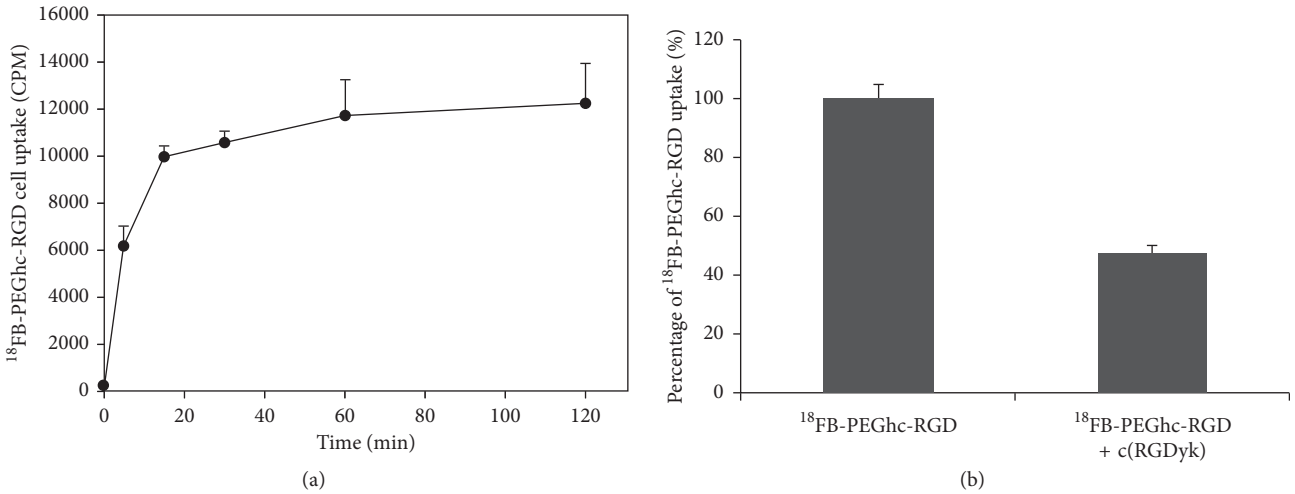

Figure 3: U87MG cell uptake (a) and inhibition study (b) of ^{18}FB-PEGHc-RGD ([^{18}F]**8**) in U87MG cells. Significant radioactivity accumulation in U87MG cells was observed in the presence of ^{18}FB-PEGHc-RGD ([^{18}F]**8**). Inhibition study using nonradiolabelled c(RGDyK) showed 52% reduction in cell uptake. Data are expressed as mean ± SD from quadruplicate samples.

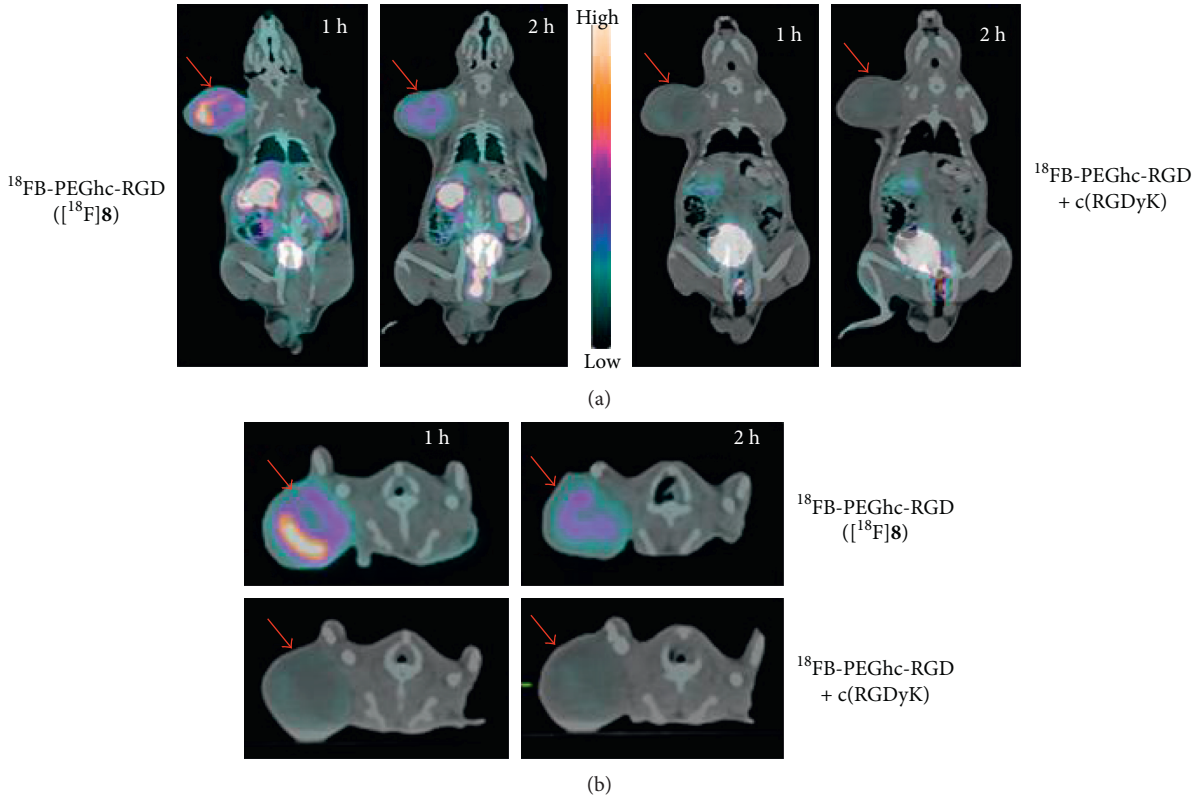

Figure 4: (a) PET/CT images of ^{18}FB-PEGHc-RGD ([^{18}F]**8**) in RR1022 tumor-bearing rats at 1 h and 2 h after injection. High radioactivity accumulations were found in the tumor (red arrow) at 1 h and 2 h after injection of ^{18}FB-PEGHc-RGD ([^{18}F]**8**). Inhibition study using nonradiolabelled c(RGDyK) showed complete blocking of radioactivity in the tumor. (b) Transaxial views showing high tumor uptake of ^{18}FB-PEGHc-RGD ([^{18}F]**8**).

10 Hz, 2H), 4.49 (t, $J = 5$ Hz, 2H), 4.08 (d, $J = 6$ Hz, 2H), and 3.79 (t, $J = 4.8$ Hz, 2H). ^{13}C NMR (100 MHz, $CDCl_3$): δ (ppm) = 167.2, 165.7, 164.7, 134.5, 132.4, 132.3, 126.5, 117.6, 115.7, 115.5, 68.1, and 64.4. FAB MS calculated for $C_{12}H_{14}O_3F_1$ was 225.0921 m/z [M + H]. It was found to be 225.0921.

*4.5. Synthesis of 5-(4-Methoxyphenyl)-2-phenyl-2H-tetrazole (**3**).* For the preparation of phenylsulfonylhydrazone [29], *p*-anisaldehyde (0.68 g, 5 mmol) was dissolved in 50 mL of ethanol and mixed with benzensulfonylhydrazide (0.86 g, 25 mmol). The mixture was stirred at room temperature for

30 min. After addition of 100 mL water, a white precipitate formed. It was separated with a filter. Diazonium salt solution was prepared by adding $NaNO_2$ (0.35 g, 5 mmol) into 2 mL of water. It was dropped into cooled aniline (0.47 g, 5.0 mmol) dissolved in 8 mL of water/ethanol (1 : 1) and 1.3 mL of concentrated hydrochloric acid (~36%). Phenylsulfonylhydrazone was dissolved in 30 mL of pyridine. Diazonium salt was then added dropwise with stirring at −10°C. A red precipitate formed after addition of 250 mL of 3NHCl. The precipitate was then collected and extracted with chloroform and water. The organic layer was dried and subjected to flash column chromatography on a silica gel (dichloromethane : ethyl acetate = 50 : 1). A red solid was obtained with a yield of 30% (382 mg).1H NMR (600 MHz, $CDCl_3$) data were δ (ppm) = 8.21 (d, J = 8.8 Hz, 4H), 7.60 (t, J = 8 Hz, 2H), 7.51 (t, J = 7.4 Hz, 1H), 7.10 (d, J = 8.8 Hz, 2H), and 3.90 (s, 3H). ^{13}C NMR (100 MHz, chloroform-d_3): δ (ppm) = 129.8, 129.6, 128.7, 119.9, 114.5, 55.6, 29.9, 22.9, and 14.3. FAB MS calculated for $C_{14}H_{13}O_1N_4$ was 253.1084 m/z [M + H]. It was found to be 253.1084.

*4.6. Synthesis of 2-((3-(4-Methoxyphenyl)-1-phenyl-4,5-dihydro-1H-pyrazol-4-yl)methoxy)ethyl 4-Fluorobenzoate (**4**).* Photoinducible 1,3-dipolar cycloaddition was performed between **2** (0.1 g, 0.4 mmol) and **3** (0.18 g, 0.79 mmol) in 16 mL of mixture of acetonitrile/PBS (50/50). The reaction mixture was irradiated with 302 nm UV lamp for 5 min, 10 min, 20 min, 30 min, 1 h, and 2 h with stirring at room temperature. After that, the mixture was extracted with chloroform and water. The organic layer was then dried. The crude mixture was then purified by flash column chromatography on silica gel (dichloromethane : ethyl acetate = 50 : 1) to obtain a product with a yield of 63% (112.4 mg). 1H NMR (600 MHz, acetonitrile-d_3): δ (ppm) = 8.02 (dd, J = 8.7 Hz, 5.4 Hz, 2H), 7.79 (dd, J = 8.1 Hz, 2.4 Hz, 2H), 7.67 (dd, J = 8.4 Hz, 1.2 Hz, 2H), 7.45 (t, J = 7.5 Hz, 2H), 7.40 (tt, J = 7.5 Hz, 1.2 Hz, 1H), 7.20 (t, J = 8.7 Hz, 2H), 6.98 (dd, J = 6.6 Hz, 22.4 Hz, 2H), 6.81 (s, 1H), 4.58 (s, 2H), 4.44 (t, J = 4.8 Hz, 2H), 3.84 (m, 4H), and 3.82 (s, 3H). ^{13}C NMR (151 MHz, acetonitrile-d_3): δ (ppm) = 166.6, 165.2, 159.8, 151.0, 140.7, 139.9, 132.2, 129.2, 127.7, 126.8, 125.8, 124.1, 115.7, 115.6, 114.4, 105.8, 67.9, 64.2, 62.9, 55.0, and 16.6. FAB MS calculated for $C_{26}H_{25}O_4N_0F_1$ was 448.1793 m/z [M]. It was found to be 448.1790.

*4.7. Synthesis of 2-((3-(4-Methoxyphenyl)-1-phenyl-4,5-dihydro-1H-pyrazol-4-yl)methoxy)ethyl 4-[^{18}F]fluorobenzoate ([^{18}F]**4**).* Photoinducible 1,3-dipolar cycloaddition was performed with **3** (1 mg, 3.96 mmol) and 2-(allyloxy) ethyl 4-[^{18}F]fluorobenzoate ([^{18}F]**2**) in 0.2 mL of acetonitrile-phosphate buffer = 1 : 1. The reaction mixture was irradiated with 302 nm UV lamp for 30 min with stirring. For purification, the reaction mixture was immediately loaded into RP-HPLC (A = 0.1% TFA in water/B = 0.1% TFA in acetonitrile, 254 nm, 3.0 mL/min) followed by gradient purification (isocratic flow with 10% B for 5 min, gradient increase from 10% → 100% B for 25 min, and maintaining the flow with 100% B for 10 min). Retention time of the desired compound was 27 min. RP-HPLC was performed for the collected peak for identification using nonlabelled standard compound. Decay-corrected radiochemical yield of [^{18}F]**4** was 36% including HPLC purification and synthesis time was 58 min.

*4.8. Synthesis of 4-(2-Phenyl-2H-tetrazol-5-yl)benzoate (**5**).* Compound **5** was prepared by a previously reported procedure [29]. To a flask containing compound 4-formylbenzoic acid (2.25 g, 15.0 mmol), ethanol (50 mL) was added. Benzoylsulfonohydrazide (2.58 g, 75.0 mmol) was added to the above solution. A white precipitate formed after addition of 150 mL water. It was collected in a funnel. The white solid was dissolved in 90 mL pyridine to give solution A. A solution of $NaNO_2$ (1.04 g, 15.0 mmol) in 6 mL water was added dropwise to a cooled mixture of aniline (1.40 g, 15.0 mmol) dissolved in 24 mL water-ethanol (1 : 1) and 4 mL concentrated HCl to give solution B. Solution B was added slowly to solution A cooled with an ice bath. The reaction mixture was then extracted with ethyl acetate (3 × 30 mL). A precipitate formed after adding 750 mL 3NHCl to the combined organic layers. It was collected and dried. The desired product was analyzed by LC/MS/MS and ^{1}H/^{13}C NMR. 1H NMR (600 MHz, chloroform-d_3): δ (ppm) = 8.27 (d, J = 4.2 Hz, 2H), 8.14 (t, J = 8.4 Hz, 4H), 7.68 (t, J = 8.4 Hz, 2H), and 7.62 (t, J = 7.2 Hz, 1H). ^{13}C NMR (100 MHz, chloroform-d_3): δ (ppm) = 167.2, 164.3, 136.6, 133.3, 130.9, 130.8, 127.3, and 120.5. LC-mass/HRMS (m/z): $[M + H]^+$ calculated for $C_{14}H_{11}N_4O_2$ was 267.0884; it was found to be 267.0885.

*4.9. Synthesis of 2,5-Dioxopyrrolidin-1-yl 4-(2-phenyl-2H-tetrazol-5-yl)benzoate (**6**).* N-hydroxysuccinimide (NHS, 86.5 mg, 0.75 mmol) was added to a mixture of 1-ethyl-3-3-dimethylaminopropylcarbodiimide (EDC, 116.7 mg, 0.75 mmol) and 4-(2-phenyl-2H-tetrazole-5-yl)-benzoic acid (100 mg, 0.38 mmol) in 5 mL acetonitrile followed by incubation at room temperature overnight with a stream of N_2 gas. The reaction mixture was then diluted with 100 mL of CH_2Cl_2 and water. The organic layer was washed three times with 100 mL of water followed by wash with 100 mL of brine once. The organic layer was dried over sodium sulfate and then evaporated. The resulting crude mixture was purified with flash column chromatography (ethyl acetate : hexane = 1 : 1). An orange powder was obtained with a yield of 21.9% (30 mg). The product was analyzed by LC/MS/MS and ^{1}H/^{13}C NMR. ^{1}H NMR (600 MHz, $CDCl_3$): δ (ppm) = 8.42 (d, J = 9 Hz, 2H), 8.29 (d, J = 9 Hz, 2H), 8.21 (d, J = 7.8 Hz, 2H), 7.59 (t, J = 15 Hz, 2H), 7.53 (t, J = 15.6 Hz, 1H), and 2.94 (s, 9H). ^{13}C NMR (151 MHz, dichloromethane-d_2): δ (ppm) = 169.8, 164.5, 162.1, 131.7, 130.6, 130.4, 127.9, 120.5, 34.5, and 26.3. LC-mass/HRMS (m/z): $[M + H]^+$ calculated for $C_{18}H_{14}N_5O_4$ was 364.1047; it was found to be 364.1040.

*4.10. Synthesis of 2,5-Dioxopyrrolidin-1-yl 4-(2-phenyl-2H-tetrozol-5-yl)benzoate-RGD Conjugate (**7**).* Cyclic Arg-Gly-Asp-D-Tyr-Lys (cRGDyK, 5.8 mg, 0.006 mmol) was

added to a mixture of **6** (5 mg, 0.01 mmol) and *N*, *N′*diisopropylethylamine -(DIPEA, 1.8 mg, 0.01 mmol) in 1 mL of dimethylformamide (DMF) followed by incubation at room temperature for two hours with a stream of N_2 gas. The mixture was purified using RP-HPLC. Flow rate was set at 2.5 ml/min. The mobile phase consisted of solvent A (0.1% trifluoroacetic acid in water) and solvent B (0.1% trifluoroacetic acid in acetonitrile). Gradient details were as follows: 0–5 min, 1% B; 5–30 min, 20% B; 30–45 min, 70% B; and 45–60 min, 100% B. Retention time of the product was 43 min. The product was analyzed by LC/MS/MS. LC-mass/HRMS (*m*/*z*): $[M+H]^+$ calculated for $C_{41}H_{50}N_{13}O_9$ was 868.3855; it was found to be 868.3848.

*4.11. Synthesis of FB-PEGhc-RGD (**8**).* A photoinducible 1,3-dipolar cycloaddition was performed between 2,5-dioxop yrrolidin-1-yl 4-(2-phenyl-2H-tetrozol-5-yl)benzoate-RGD (2, 1.0 mg, 0.001 mmol) and 2-(allyloxy)ethyl 4-fluorobenzoate (3.8 mg, 0.017 mmol) in 200 μL of mixture of acetonitrile/PBS (50/50). The reaction mixture was irradiated with 302 nm UV lamp for 30 min with stirring at room temperature. The mixture was purified using RP-HPLC. The flow rate was set at 3 mL/min with mobile phase consisting of solvent A (0.1% trifluoroacetic acid in water) and solvent B (0.1% trifluoroacetic acid in acetonitrile). Gradient details were as follows: 0 min, 30% B; 0–22 min, 100% B; and 22–23 min, 30% B. The retention time was 8.5 min. The desired product was analyzed by LC/MS/MS. LC-mass/HRMS (*m*/*z*): $[M+H]^+$ calculated for $C_{53}H_{63}FN_{11}O_{12}$ was 1064.4642; it was found to be 1064.4287.

*4.12. Synthesis of ^{18}FB-PEGhc-RGD ([^{18}F]**8**).* Photoinducible 1,3-dipolar cycloaddition was performed by mixing 2,5-dioxopyrrolidin-1-yl 4-(2-phenyl-2H-tetrozol-5-yl)benzoate-RGD (1 mg) and 2-(allyloxy)ethyl 4-[^{18}F]fluorobenzoate in 0.2 ml of acetonitrile-phosphate buffer at 1 : 1. The reaction mixture was irradiated with 302 nm UV lamp for 30 min with stirring. The reaction mixture was purified using RP-HPLC. The flow was at 3 mL/min. Mobile phase consisted of solvent A (0.1% trifluoroacetic acid in water) and solvent B (0.1% trifluoroacetic acid in acetonitrile). Gradient details were as follows: 0 min, 30% B; 0–22 min, 100% B; and 22–23 min, 30% B. Retention time of the desired compound was 8.5 min. Decay-corrected radiochemical yield of [^{18}F]**8** was 10–12% ($n = 4$), and total synthesis time was 134 min including HPLC purification and reformulation.

4.13. Tumor Cell Uptake Assay. U87MG human glioma cells were maintained and subcultured every other day in Roswell Park Memorial Institute (RPMI) 1640 media supplemented with 10% fetal bovine serum and 1% penicillin-streptomycin at 37°C in 5% CO_2 and 95% air environment. The cells were seeded into 24-well plates at density of 5×10^4 cells/well and cultured overnight. The cells were rinsed once with PBS followed by addition of [^{18}F]**8** (~0.33 MBq/well) or RGD (100 μM/well) to cultured wells in quadruplicate. After incubation at 37°C for 5, 15, 30, 60, and 120 min, cells were rinsed twice with cold PBS and harvested after treatment with TrypLE. The cells were collected in measurement tubes for counting. Finally, radioactivity of the cells was measured using a gamma counter. All experiments were performed in quadruplicate. Results are expressed as mean ± SD.

4.14. In Vivo Experiments

4.14.1. Tumor Models. All experimental protocols with animals were performed in compliance with the policies and procedures of the Institutional Animal Care and Use Committee of Chonbuk National University (Jeonju, Korea). Four male SD rats were purchased from Orient-Bio (Seoul, Korea) at 13 weeks of age. They were injected subcutaneously (s.c.) in the right flank with 1×10^7 RR1022 fibrosarcoma cells suspended in 150 μL RPMI 1640 medium. When tumors reached 0.8–1.0 cm in diameter (7 d after inoculation), rats were used for microPET imaging experiment.

4.14.2. MicroPET Studies. MicroPET scans and image data analysis were performed using a Biograph TruePoint 40 PET/CT scanner (Siemens Medical Solutions, Knoxville, TN, USA). Rat bearing RR1022 tumor was tail-vein injected with 5.1 MBq of [^{18}F]**8** under zoletil anesthesia (mg/kg). Ten-minute static PET images were then acquired at two time points (1 h and 2 h) after injection. CT scan was obtained first by a continuous spiral technique (120 kVp, 200 Ma, 0.5 s rotation time). A PET scan was then acquired in 3-dimensional mode at 15 minutes per bed position. Obtained PET data were reconstructed iteratively using an ordered-subset expectation maximization algorithm. Initial CT data were used for attenuation correction. For receptor-blocking experiment, c(RGDyK) (10 mg/kg) was coinjected with 5.4 MBq of [^{18}F]**8** to RR1022 tumor rat. At 1 h and 2 h after injection, ten-minute static microPET scans were acquired. Assessment of tracer distribution in tumor tissue was expressed as tumor-to-muscle (T/M) ratio, dividing the mean activity within the ROI of the tumor by the mean activity within thigh muscle ROI.

Conflicts of Interest

The authors declare no conflicts of interest.

Authors' Contributions

Ji Hae Choi and Doori Oh contributed equally to this work.

Acknowledgments

The authors thank Kyu Young Jeong for technical assistance. This work was supported by Grant nos. 2012M2A2A7014020 and 2015M2A2A6A04044884 of the National Research Foundation funded by the Ministry of Science, ICT and Future Planning, Republic of Korea, and Business for Academic-Industrial Cooperative Establishments funded by Korea Small and Medium Business Administration in 2015.

This paper was supported by the Fund of Biomedical Research Institute, Chonbuk National University Hospital.

References

[1] H. R. Herschman, "Molecular imaging: looking at problems, seeing solutions," *Science*, vol. 302, no. 5645, pp. 605–608, 2003.

[2] S. L. Pimlott and A. Sutherland, "Molecular tracers for the PET and SPECT imaging of disease," *Chemical Society Reviews*, vol. 40, no. 1, pp. 149–162, 2011.

[3] T. F. Massoud and S. S. Gambhir, "Molecular imaging in living subjects: seeing fundamental biological processes in a new light," *Genes & Development*, vol. 17, no. 5, pp. 545–580, 2003.

[4] M. E. Phelps, "Positron emission tomography provides molecular imaging of biological processes," *Proceedings of the National Academy of Sciences*, vol. 97, no. 16, pp. 9226–9233, 2000.

[5] A. Saraste, S. G. Nekolla, and M. Schwaiger, "Cardiovascular molecular imaging: an overview," *Cardiovascular Research*, vol. 83, no. 4, pp. 643–652, 2009.

[6] P. McGeer and E. McGeer, "The inflammatory response system of brain: implications for therapy of Alzheimer and other neurodegenerative diseases," *Brain Research Reviews*, vol. 21, no. 2, pp. 195–218, 1995.

[7] M. Reivich, D. Kuhl, A. Wolf et al., "Measurement of local cerebral glucose metabolism in man with 18F-2-fluoro-2-deoxy-d-glucose," *Acta Neurologica Scandinavica: Supplementum*, vol. 64, pp. 190-191, 1977.

[8] S. S. Gambhir, "Molecular imaging of cancer with positron emission tomography," *Nature Reviews Cancer*, vol. 2, no. 9, pp. 683–693, 2002.

[9] S. M. Ametamey, M. Honer, and P. A. Schubiger, "Molecular imaging with PET," *Chemical Reviews*, vol. 108, no. 5, pp. 1501–1516, 2008.

[10] D. O'Hagan, "Understanding organofluorine chemistry: an introduction to the C-F bond," *Chemical Society Reviews*, vol. 37, no. 2, pp. 308–319, 2008.

[11] G. Vaidyanathan and M. R. Zalutsky, "Labeling proteins with fluorine-18 using N-succinimidyl 4-[^{18}F]fluorobenzoate," *International Journal of Radiation Applications and Instrumentation: Part B: Nuclear Medicine and Biology*, vol. 19, no. 3, pp. 275–281, 1992.

[12] S. Guhlke, H. H. Coenen, and G. Stocklin, "Fluoroacylation agents based on small nca [F-18]fluorocarboxylic acids," *Applied Radiation and Isotopes*, vol. 45, no. 6, pp. 715–727, 1994.

[13] P. Johnström, J. C. Clark, J. D. Pickard, and A. P. Davenport, "Automated synthesis of the generic peptide labelling agent *N*-succinimidyl 4-[^{18}F]fluorobenzoate and application to ^{18}F-label the vasoactive transmitter urotensin-II as a ligand for positron emission tomography," *Nuclear Medicine and Biology*, vol. 35, no. 6, pp. 725–731, 2008.

[14] J. Toretsky, A. Levenson, I. N. Weinberg, J. F. Tait, A. Uren, and R. C. Mease, "Preparation of F-18 labeled annexin V: a potential PET radiopharmaceutical for imaging cell death," *Nuclear Medicine and Biology*, vol. 31, no. 6, pp. 747–752, 2004.

[15] G. Vaidyanathan and M. R. Zalutsky, "Synthesis of *N*-succinimidyl 4-[^{18}F]fluorobenzoate, an agent for labeling proteins and peptides with ^{18}F," *Nature Protocols*, vol. 1, no. 4, pp. 1655–1661, 2006.

[16] B. Kuyhnast, B. Bruin, F. Hinnen, B. Tavitian, and F. Dolle, "Design and synthesis of a new [^{18}F]fluoropyridine-based haloacetamide reagent for the labeling of oligonucleotides: 2-bromo-*N*-[3-(2-[18F]fluoropyridin-3-yloxy)propyl]acetamide," *Bioconjugate Chemistry*, vol. 15, no. 3, pp. 617–627, 2004.

[17] E. von Guggenberg, J. A. Sader, J. S. Wilson et al., "Automated synthesis of an ^{18}F-labelled pyridine-based alkylating agent for high yield oligonucleotide conjugation," *Applied Radiation and Isotopes*, vol. 67, no. 9, pp. 1670–1675, 2009.

[18] B. Kühnast, F. Dollé, F. Vaufrey, F. Hinnen, C. Crouzel, and B. Tavitian, "Fluorine-18 labeling of oligonucleotides bearing chemically-modified ribose-phosphate backbones," *Journal of Labelled Compounds and Radiopharmaceuticals*, vol. 43, no. 8, pp. 837–848, 2000.

[19] B. Kuhnast, F. Hinnen, R. Hamzavi et al., "Fluorine-18 labelling of PNAs functionalized at their pseudo-peptidic backbone for imaging studies with PET," *Journal of Labelled Compounds and Radiopharmaceuticals*, vol. 48, no. 1, pp. 51–61, 2005.

[20] R. Huisgen, 1,3-Dipolar Cycloaddition Chemistry, A. Padwa, Ed., Vol. 1, Wiley, New York, NY, USA, 1984.

[21] H. C. Kolb, M. G. Finn, and K. B. Sharpless, "Click chemistry: diverse chemical function from a few good reactions," *Angewandte Chemie International Edition*, vol. 40, no. 11, pp. 2004–2021, 2001.

[22] V. D. Bock, H. Hiemstra, and J. H. van Maarseveen, "Cu(I) catalyzed alkyne–azide "click" cycloadditions from a mechanistic and synthetic perspective," *European Journal of Organic Chemistry Banner*, vol. 2006, no. 1, pp. 51–68, 2006.

[23] J. Marik and J. L. Sutcliffe, "Click for PET: rapid preparation of [^{18}F]fluoropeptides using Cu(I) catalyzed 1,3-dipolar cycloaddition," *Tetrahedron Letters*, vol. 47, no. 37, pp. 6681–6684, 2006.

[24] D. H. Kim, Y. S. Choe, and B. T. Kim, "A ^{18}F-labeled glucose analog: synthesis using a click labeling method and in vivo evaluation," *Applied Radiation and Isotopes*, vol. 68, no. 2, pp. 329–333, 2010.

[25] C. M. Lee, H. J. Jeong, D. W. Kim, M. H. Sohn, and S. T. Lim, "The effect of fluorination of zinc oxide nanoparticles on evaluation of their biodistribution after oral administration," *Nanotechnology*, vol. 23, no. 20, pp. 205102–205108, 2012.

[26] V. Bouvet, M. Wuest, and F. Wuest, "Copper-free chemistry with the short-lived positron emitter fluorine-18," *Organic & Biomolecular Chemistry*, vol. 9, no. 21, pp. 7393–7399, 2011.

[27] L. S. Campbell-Verduyn, L. Mirfeizi, A. K. Schoonen, R. A. Dierckx, P. H. Elsinga, and B. L. Feringa, "Strain-promoted copper-free "click" chemistry for ^{18}F radiolabeling of bombesin," *Angewandte Chemie International Edition*, vol. 50, no. 47, pp. 11117–11120, 2011.

[28] Y. Wang, C. I. Vera, and Q. Lin, "Convenient synthesis of highly functionalized pyrazolines via mild, photoactivated 1,3-dipolar cycloaddition," *Organic Letters*, vol. 9, no. 21, pp. 4155–4158, 2007.

[29] W. Song, Y. Wang, J. Qu, M. M. Madden, and Q. Lin, "A photoinducible 1,3-dipolar cycloaddition reaction for rapid, selective modification of tetrazole-containing proteins," *Angewandte Chemie International Edition*, vol. 47, no. 15, pp. 2832–2835, 2008.

[30] R. K. V. Lim and Q. Lin, "Photoinducible bioorthogonal chemistry: a spatiotemporally controllable tool to visualize and perturb proteins in live cells," *Accounts of Chemical Research*, vol. 44, no. 9, pp. 828–839, 2011.

[31] H. M. Sheldrake and L. H. Patterson, "Function and antagonism of β integrins in the development of cancer therapy," *Current Cancer Drug Targets*, vol. 9, no. 4, pp. 519–540, 2009.

[32] K. Temming, R. M. Schiffelers, G. Molema, and R. J. Kok, "RGD-based strategies for selective delivery of therapeutics and imaging agents to the tumour vasculature," *Drug Resistance Updates*, vol. 8, no. 6, pp. 381–402, 2005.

[33] G. Vaidyanathan, B. J. White, and M. R. Zalutsky, "Propargyl 4-[^{18}F]fluorobenzoate: a putatively more stable prosthetic group for the fluorine-18 labeling of biomolecules via click chemistry," *Current Radiopharmaceuticalse*, vol. 2, no. 1, pp. 63–74, 2009.

Hindawi
Contrast Media & Molecular Imaging
Volume 2018, Article ID 8969714, 9 pages
https://doi.org/10.1155/2018/8969714

Research Article

Noninferiority of ^{99m}Tc-Ethylenedicysteine-Glucosamine as an Alternative Analogue to ^{18}F-Fluorodeoxyglucose in the Detection and Staging of Non-Small Cell Lung Cancer

Dong Dai,[1] **F. David Rollo**,[2] **Jerry Bryant**,[2] **and E. Edmund Kim**[3,4]

[1] *Tianjin Medical University Cancer Institute and Hospital, Tianjin, China*
[2] *Cell➤Point Biotechnology, Centennial, CO, USA*
[3] *University of Texas MD Anderson Cancer Center, Houston, TX, USA*
[4] *University of California, Irvine, CA, USA*

Correspondence should be addressed to Dong Dai; dongdai@tmu.edu.cn

Received 8 November 2017; Accepted 30 January 2018; Published 15 March 2018

Academic Editor: Ralf Schirrmacher

Objective. ^{99m}Tc-ethylenedicysteine-glucosamine (^{99m}Tc-EC-G) was developed as a potential alternative to ^{18}F-FDG for cancer imaging. A Phase 2 study was conducted to compare ^{18}F-FDG PET/CT and ^{99m}Tc-EC-G SPECT/CT in the detection and staging of patients with non-small cell lung cancer (NSCLC). This study was aimed to demonstrate that ^{99m}Tc-EC-G SPECT/CT was not inferior to ^{18}F-FDG PET/CT in patients with confirmed NSCLC. *Methods.* Seventeen patients with biopsy proven NSCLC were imaged with ^{99m}Tc-EC-G and ^{18}F-FDG to detect and stage their cancers. Imaging with PET/CT began 45–60 minutes after injection of ^{18}F-FDG. Imaging with ^{99m}Tc-EC-G began at two hours after injection (for 5 patients) or three hours (for 12 patients). SPECT/CT imaging devices from the three major vendors of SPECT/CT systems were used at 6 participating study sites. The image sets were blinded to all clinical information and interpreted by independent PET and SPECT expert readers at a central independent core laboratory. *Results.* 100% concordance between ^{99m}Tc-EC-G and ^{18}F-FDG for primary lesion detection, lesion location and size, and confidence that the biopsied lesion was malignant. There was 70% agreement between ^{99m}Tc-EC-G and ^{18}F-FDG for metastatic lesion detection, location and size, and confidence that the suspicious lesions were malignant. *Conclusions.* Evaluation of primary and suspicious metastatic lesions detected by ^{99m}Tc-EC-G and ^{18}F-FDG on 17 patients resulted in excellent agreement for detection of primary and metastatic lesions. The study results indicated that ^{99m}Tc-EC-G SPECT/CT has the potential to be a clinically viable alternative to ^{18}F-FDG PET/CT and ^{99m}Tc-EC-G is not inferior to ^{18}F-FDG PET/CT.

1. Introduction

1.1. Molecular Mechanism of Ethylenedicysteine-Glucosamine (EC-G) in Oncology. ^{18}F-Fluoro-2-deoxyglucose (FDG), a nonmetabolizable 2-deoxyglucose analogue, blocks glycolysis and inhibits protein glycosylation [1]. Increased ^{18}F-FDG uptake is used to visualize cancer cells in patients using PET/CT [2, 3]. In addition, it is known that cell uptake of glucose and glutamine is directed by growth factor signaling. Both glucose and glutamine are involved in mitochondrial tricarboxylic acid (TCA) cycle integrity, glycolysis, ATP production, and glycosylation [4, 5]. For example, glutamine is a known precursor amino acid for the synthesis of O-linked-Beta N-acetylglucosamine (GlcNAc), one of the main initiators of the Hexosamine Biosynthetic Pathway (HBP) [6–8]. Glutamine combines with fructose-6-phosphate from the glucose glycolytic pathway in the presence of glutamine fructose-6-phosphate transferase (GFAT), an initiating enzyme, resulting in the synthesis of glucosamine-6-phosphate [7, 8]. A series of enzymatic steps result in the production of uridine diphosphate-N-acetylglucosamine (UDP-GlcNAc) in endoplasmic reticulum (ER). The synthesized UDP-GlcNAc is transported from ER to the Golgi apparatus via the UDP-GlcNAc transporters and is then utilized as a donor substrate for the *N*- and *O*-linked glycosylation of extracellular and membrane proteins

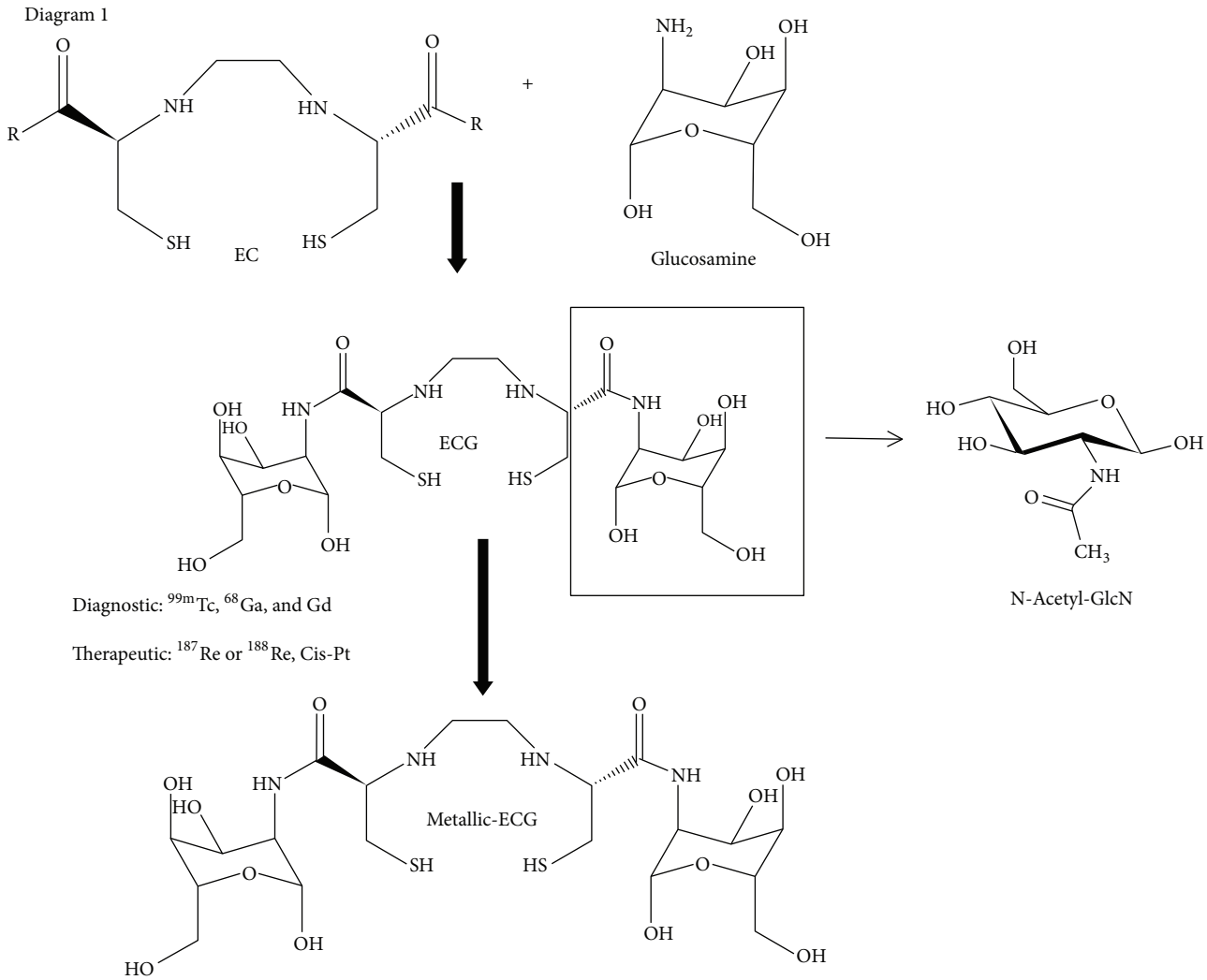

Figure 1: Structure of ethylenedicysteine-glucosamine (EC-G) and relationship to N-acetylglucosamine (GlcNAc).

[9, 10]. O-linked glycosylation is regulated by the terminating enzyme O-linked GlcNAc transferase (OGT). OGT is the enzyme responsible for the addition of a single N-acetylglucosamine (GlcNAc) residue to the hydroxyl groups of serine and/or threonine residues of target proteins. The hexosamine signaling pathway terminating in O-linked GlcNAc cycling has been shown to be involved in cellular signaling cascades and regulation of transcription factors involved in cancer biology and is a requirement for cell membrane and protein synthesis for cell regeneration in other tissue types as well [10–12]. GlcNAc, a glucose analogue, can be taken up by cells through glucose transporters [13, 14]. In cancer cells, GlcNAc glycosylation has been shown to play a role of angiogenesis and metastasis [12]. We have then developed a metabolic agent that mimics GlcNAc pathway by combining the chelator, ethylenedicysteine (EC), to two molecules of D-glucosamine [15–17] creating the chemical analogue ethylenedicysteine-glucosamine (EC-G), a metabolic conjugate compound containing two molecules of GlcNAc [18]. The molecular mechanism of EC-G involves trapping by phosphorylation, docking by UDP conjugation at position-1 of glucosamine, fusing by recruiting NfKb protein conjugation at position-1 of glucosamine, and translocation of fused glycoprotein to cell nuclei to regulate Sp1 and myc [19–21]. In addition to its application in molecular diagnostic imaging, EC-G binds to therapeutic metals that can be used to treat cancer cells (Figure 1).

1.2. Cellular Uptake Differences between ^{99m}Tc-EC-G and ^{18}F-FDG. It is well known that ^{18}F-FDG localizes in inflammatory cells [14] and infection [15]. Glucose loading studies were performed with stimulated macrophages and neutrophils for both ^{99m}Tc-EC-G and ^{18}F-FDG (Figures 2 and 3). It can be seen that increasing the concentration of glucose in the presence of macrophages or neutrophils results in a decrease in ^{18}F-FDG uptake due to competition between ^{18}F-FDG and glucose. Alternatively, ^{99m}Tc-EC-G uptake in macrophages or neutrophils is minimal and remains constant independent of the amount of glucose loading. This suggests the potential for ^{99m}Tc-EC-G to have increased diagnostic accuracy over ^{18}F-FDG in patients having an infectious process such as tuberculosis, pneumonia, or a granulomatous

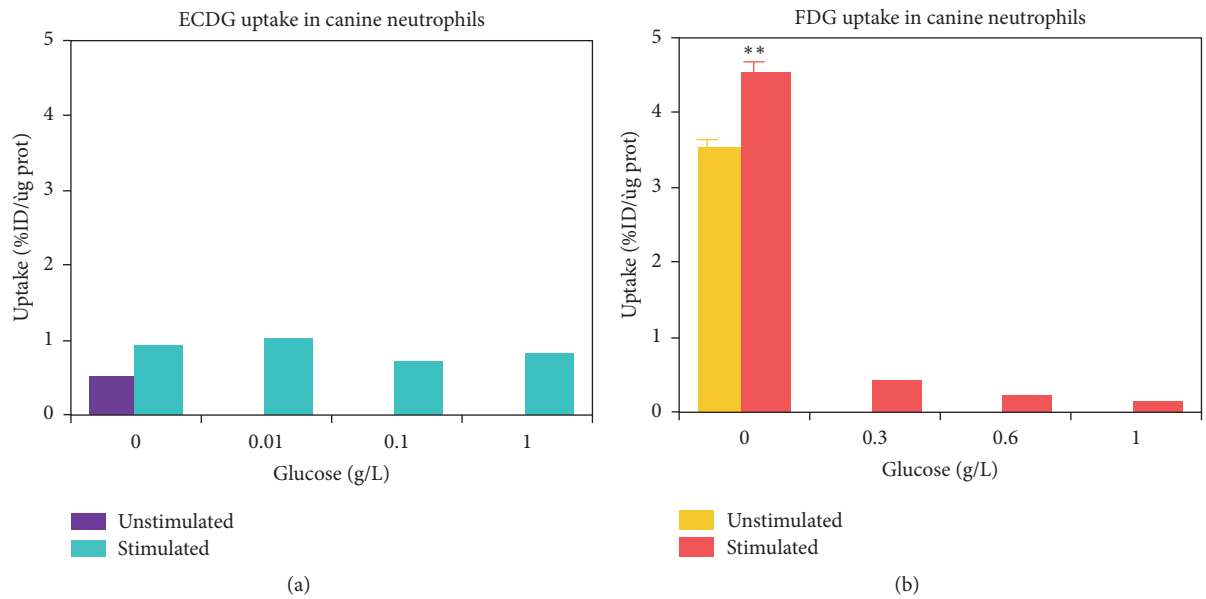

Figure 2: Comparative uptake of ^{99m}Tc-EC-G versus ^{18}F-FDG in stimulated neutrophils as a function of glucose concentration (Courtesy of Alexis Broisat and Dr. David K. Glover: Department of Medicine, Cardiovascular Division, University of Virginia, Charlottesville, VA). ∗∗ indicates a significant uptake difference ($P < 0.05$, t-test) between glucose loading and control groups.

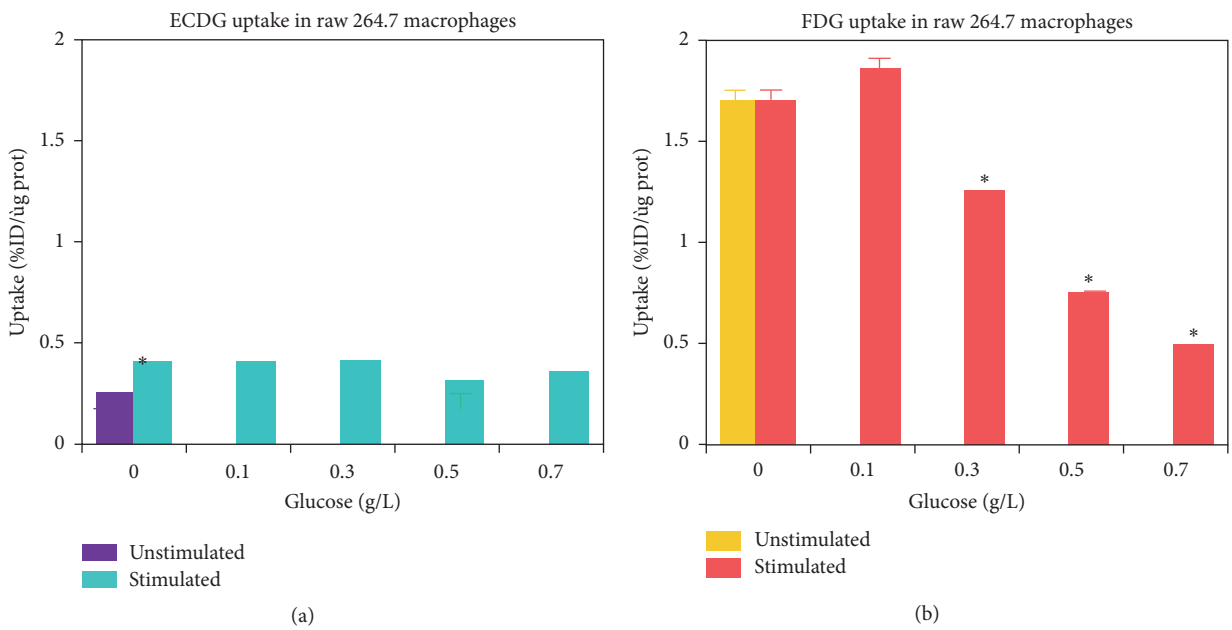

Figure 3: Comparative uptake of ^{99m}Tc-EC-G versus ^{18}F-FDG in stimulated macrophages as a function of glucose concentration (Courtesy of Alexis Broisat and Dr. David K. Glover: Department of Medicine, Cardiovascular Division, University of Virginia, Charlottesville, VA). ∗ indicates a significant uptake difference ($P < 0.05$, t-test) between glucose loading and control groups.

disease. ^{99m}Tc-EC-G should have a clear advantage compared to ^{18}F-FDG in evaluating the efficacy of therapy in real time while the patient is undergoing therapy. The reason is the inflammatory reaction of the collateral tissue surrounding the tumor following the initiation of chemotherapy or radiation therapy. Consequently, an ^{18}F-FDG PET/CT imaging procedure is not able to differentiate between the inflammation and the impact of the therapy on the tumor because the tumor is obfuscated by the presence of the inflammation.

^{99m}Tc-EC-G localizes in the nucleus of cells. Several experiments, which were proof of concept studies, demonstrated intranuclear localization that was validated by performing cytosol studies as well as thymidine incorporation studies [13]. The results of cytosol study showed ^{18}F-FDG

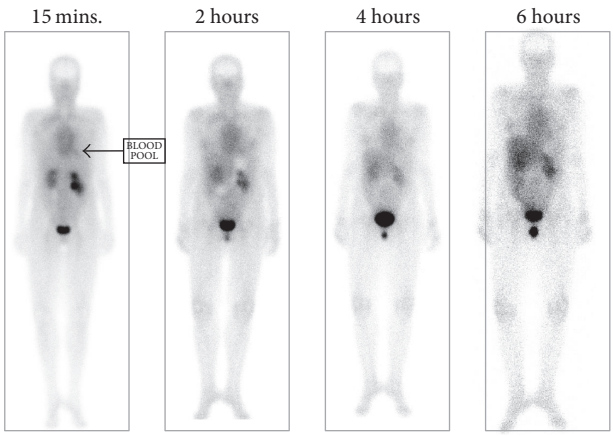

Figure 4: Whole-body planar biodistribution images of ^{99m}Tc-EC-G at 15, 30, 60, 120, and 240 minutes after injection. Note absence of activity in the brain, heart, and bone.

to be localized completely within the cytoplasm whereas the ^{99m}Tc-EC-G localized in the nucleus. The thymidine incorporation studies showed that glucose and ^{99m}Tc-EC-G localize in all three phases of cell proliferation (G0/G1, G2/M, and S), while there was no uptake of ^{18}F-FDG in any of the phases of cell proliferation [13]. This suggests that EC-G (GlcNAc) and glucose are both involved in the proliferation/growth activity of the cells, whereas ^{18}F-FDG is not in glycosylation process. Lack of ^{18}F-FDG activity in the proliferation and growth studies is attributed to the location of the fluorine atom in position 2 of the molecule, which prevents acetylation occurrence and is recognized by UDP and participation in cell proliferation and growth.

1.3. Metallic Application with EC-G. Using a chelator such as EC, radiodiagnostic (^{99m}Tc, ^{111}In, and ^{68}Ga), radiotherapeutic (^{177}Lu, ^{188}Re, ^{90}Y, ^{225}Ac, and ^{223}Ra), and nonradioactive metals (^{187}Re, Pt, and Cu) have the opportunities to be incorporated. Thus, for both diagnostic and therapeutic metallic labels, EC-G is considered as a new theranostic molecule.

1.4. ^{99m}Tc-EC-G Characteristics in Oncology (Phase 1 Finding). Planar biodistribution images of ^{99m}Tc-EC-G (Figure 4) from our Phase 1 study are hallmarked by no uptake in the normalized bone, brain, or myocardium. In addition, there is minimal uptake in the liver until late in the imaging cycle. This demonstrates a different biodistribution pattern compared to ^{18}F-FDG, which has significant uptake in the normalized heart, brain, and bone marrow. It is postulated that the absence of ^{99m}Tc-EC-G uptake in the normal brain is due to the charge on the EC-G which prevents the compound from crossing the blood-brain barrier. However, in the presence of a tumor lesion, the uptake in the region(s) of abnormality should occur. Thus, a ^{99m}Tc-EC-G whole-body scan, which would include the brain, could potentially be used to determine if brain metastasis is present. To extend evidence of ^{99m}Tc-EC-DG imaging efficacy in identifying anatomical regions and in determining extent of disease in these patients as compared to ^{18}F-FDG PET/CT imaging, here, we report a multicenter Phase 2 study comparing ^{99m}Tc-EC-G SPECT/CT with ^{18}F-FDG PET/CT in patients with non-small cell lung cancer (NSCLC).

2. Materials and Methods

2.1. Primary Endpoint and Objectives. CGMP grade EC-G was manufactured at J-STAR Research, Inc. (South Plainfield, New Jersey). ^{99m}Tc-EC-G was delivered by the local radiopharmacy to the clinical trial site. The endpoints for this Phase 2 study were as follows:

(1) Noninferior to the sensitivity of ^{99m}Tc-EC-G SPECT/CT versus ^{18}F-FDG PET/CT for the biopsied primary tumor.

(2) Noninferior to the detectability and confidence level for determining malignancy/or not for metastatic disease using ^{99m}Tc-EC-G SPECT/CT versus ^{18}F-FDG PET/CT.

The Phase 2 trial was a multicenter study conducted on a total of 22 untreated patients (12 women and 10 men) aged 46.4 to 89.5 years (mean age: 68.5), who had noninvasive biopsy-definitive evidence of NSCLC or cytology results confirming NSCLC from a bronchoscope procedure. Patients underwent imaging procedures with both ^{99m}Tc-EC-G SPECT/CT and ^{18}F-FDG PET/CT. Of the 22 enrolled patients, 17 patients completed the study.

Within 7 days of qualification for the study or during prestudy procedures, ^{18}F-FDG was administered and a PET/CT scan was performed. A dose range of 370 to 740 MBq of ^{18}F-FDG was injected into a peripheral vein of the upper extremity (actual dose administered was to be consistent with the recommendations of the vendor of the PET/CT system). A CT scan without contrast from the base of the skull to the upper thigh level was acquired 60 minutes following injection of the ^{18}F-FDG. This was used for attenuation correction (AC). Alternatively, a High Quality CT Scan (HQS) sufficient to provide an AC map and adequate for anatomical localization when fused with the PET image could have been substituted for the attenuation correction CT scan. Whole-body PET imaging from the base of the skull to the upper thigh level was immediately obtained after the attenuation correction CT scan or the alternative HQS. If the HQS alternative was not utilized, the PET scan was followed by a diagnostic CT scan (without contrast from base of skull to upper thigh level). This CT scan was used for anatomical localization. Standard practice imaging protocols were used unless otherwise specified or clinically indicated.

^{99m}Tc-EC-G was administered and a SPECT/CT scan performed from 1 to 3 days following the PET/CT scan (or within 45 days if the PET/CT scan was done as a part of prestudy procedures). A target activity level of 925 MBq (range from 740 to 1110 MBq) of ^{99m}Tc-EC-G was administered through an indwelling IV line. The dose of EC-G was approximately

5 mg for the first 5 enrolled patients and approximately 1 mg or less for the remaining 12 patients. A HQS without contrast from the base of the skull to the upper thigh level (covering the same field of view as the PET/CT scan) was acquired approximately 2 hours following injection of 5 mg of ^{99m}Tc-EC-G and at approximately 3 hours following injection of the 1 mg (or less) dose of ^{99m}Tc-EC-G. The CT information was used to create an attenuation correction map for the attenuation correction, whereas the HQS was fused with the SPECT images to provide anatomical localization of lesions. Immediately after the HQS was performed, the patient was given a SPECT scan from the base of the skull to the upper thigh level. Standard practice imaging protocols were used unless otherwise specified or clinically indicated.

After the last imaging procedure, a 21-day follow-up was performed (without a patient visit) to acquire any additional imaging, surgical/pathology tissue diagnostic results, and treatment documentation. Safety was evaluated by assessing vital signs, EKGs, physical examinations, clinical laboratory test results, and the incidence and severity of AEs.

3. Statistical Considerations

3.1. Overview. The Phase 2 study was designed to be exploratory and include up to 25 patients with a biopsy (or cytology report from a bronchoscope) definitive diagnosis for NSCLC. The study design included 7 centers with no more than 8 patients completing the entire protocol at any center. This number of patients was considered sufficient to obtain the necessary data and knowledge to document continued safe use of ^{99m}Tc-EC-G in multiple centers and to organize and plan a Phase 3 study.

3.2. Core Lab Interpretation Process: Independent Reading. The endpoints for this study include estimates of agreement (based on anatomical location and measures of extent of disease (staging) above and below the diaphragm) between PET/CT and SPECT/CT. The first endpoint was ^{99m}Tc-EC-G SPECT/CT not being inferior to ^{18}F-FDG PET/CT based on tissue specific pathology results for the primary lesion. In terms of the primary lesion, tissue specimens with a pathological diagnosis of malignancy were classified as positive. Any other pathology results, such as benign or inflammatory conditions, were classified as negative. The second endpoint was ^{99m}Tc-EC-G SPECT/CT not being inferior to ^{18}F-FDG PET/CT in the detection of suspicious malignant lesions (metastasis). Measures were based on detectability of suspicious lesions in one or more of the following anatomical zones: lobes for the right and left lungs; the mediastinum; the liver; and the adrenal glands.

A five-page interpretation form was completed by each core laboratory independent reader for each image set performed on each patient. The image interpretation was based on an objective score 1–5 with 5 representing the highest positive score, where the reader evaluated the following factors:

Diagnostic image quality above and below the diaphragm

Detectability of primary lesion and confidence that it represents cancer

Detectability of any suspicious metastatic lesions and the anatomical zone for the lesion as well as the confidence that the lesion represents a malignancy

Lesion size, scored as a range (1: <5 mm; 2: 5 mm–1 cm; 3: >1 cm)

The SPECT/CT image sets were read and interpreted by two dedicated independent SPECT specialists. Separately, the PET/CT image sets were read and interpreted by two dedicated independent PET specialists. All reads were blinded to clinical information other than knowing all patients enrolled had positive tissue diagnosis of NSCLC for the primary lesion.

When PET and/or SPECT readers at the core laboratory identified suspicious lesions beyond the primary (biopsied) lesion, they scored lesion detectability, identified the anatomical location and lesion size, and recorded their confidence that the lesion(s) was (were) malignant. When more than one lesion was identified in a given anatomical zone, the reader was instructed to evaluate the single lesion they felt best represented the diagnosis for the group. The objective results were provided to the biostatistician to perform the noninferiority analysis comparing the ^{99m}Tc-EC-G SPECT/CT results to the ^{18}FDG PET/CT results for detecting primary as well as metastatic lesions on patients who had a confirmed biopsy proven diagnosis of NSCLC.

4. Results

4.1. Safety. All AEs that were reported during the study occurred after the administration of ^{99m}Tc-EC-G. All but 2 AEs, nausea and vomiting, were considered unrelated to the study drug. These 2 AEs for nausea and vomiting occurred in 1 patient after administration of ^{99m}Tc-EC-G and were classified as mild and unlikely related to the study drug. Most AEs were classified as mild or moderate, with 3 AEs (international normalized ratio increased, hypokalemia, and embolism) in 2 patients being classified as severe. There were 6 SAEs (obstructive pneumonia, hypokalemia, international normalized ratio increased to 2 times the upper limit of normal, ataxia, speech impairment, and embolism) in 3 patients. All moderate and severe AEs were evaluated and deemed by the Safety Panel to be unrelated to the study drug. Overall, ^{99m}Tc-EC-G and ^{18}F-FDG were well tolerated.

4.2. Imaging Results

4.2.1. Primary Lesion. The ^{18}FDG PET/CT and ^{99m}Tc-EC-G SPECT/CT scan results showed 100% concordance for detection of primary lesions, determination of lesion size, and confidence that the detected lesion was malignant. The detection of primary lesions was not influenced by the dose of ^{99m}Tc-EC-G or by the time of imaging in the range of doses and times used in the 2 studies. The detection of the primary lesion was also not influenced by the type of imaging device or the device vendor (imaging devices from the three major

international vendors were used in the study). Overall, the study results demonstrated noninferior detection of primary lesions (biopsied) of ^{99m}Tc-EC-G SPECT/CT compared to ^{18}F-FDG PET/CT (sensitivity only). The reader's average score [1–5] for detectability, lesion location and lesion size, and confidence that the lesion was malignant averaged 4.6 for the PET readers and 4.5 for the SPECT readers.

There was 1 patient who entered the Phase 2 study with a negative biopsy for NSCLC. However, this patient smoked, showed all of the clinical symptoms for lung cancer (e.g., blood in sputum), and had diagnostic findings on the CT scan that the radiologist felt were consistent with a diagnosis of a lung malignancy. The radiologist recommended that the referring physician order a ^{18}F-FDG PET/CT scan. The decision was made to also perform a ^{99m}Tc-EC-G SPECT/CT scan which also showed a positive finding. Based on the positive results of the ^{18}F-FDG PET/CT scan, the patient was sent to surgery for tumor removal, and the extracted tumor was found positive for NSCLC. In this case, the use of ^{18}F-FDG PET/CT and separately ^{99m}Tc-EC-G SPECT/CT scanning both achieved an accurate diagnosis even in light of the original negative biopsy. This example shows the value of oncology imaging to assure patients receive the correct diagnosis and therefore the most appropriate therapy.

4.2.2. Metastatic Lesions. Metastatic lesions were also shown to localize ^{99m}Tc-EC-G for both the 1 and 5 mg dose of EC-G. However, the detectability of some lesions in dense tissue such as the liver and adrenal glands was shown to be affected by the characteristics of the SPECT/CT system used. Specifically, lesion detectability with select SPECT/CT systems was at a lower confidence level compared to PET/CT. This occurred on two SPECT/CT systems where the slice thickness used to reconstruct the AC map and fuse the SPECT and CT images was 1 cm. Unfortunately, these two devices accounted for all reported lesions in the liver (3 lesions) and adrenal glands (1 lesion). This occurred because the 1 cm slice thickness used for the reconstruction of the AC maps resulted in artifacts and distortion of the SPECT/CT fused image. This of course impacted image quality and detectability of small lesions. Despite this issue, there was 70% overall agreement between SPECT/CT and PET/CT for all metastatic lesions. There was 83% agreement for metastatic lesions detected in the lungs (10/12 lesions), 75% agreement for lesions in the mediastinum (3/4 lesions), 66% agreement for liver lesions (2/3), and 0% agreement for adrenal lesions (0/1). Retrospectively, it was reported that the suspicious adrenal lesion was a midline abdominal lesion that had a confirmed diagnosis of pancreatitis and one suspicious lung met was confirmed as a granulomatous infection. Even without this retrospective information, when there was agreement, the confidence level for PET/CT was 4.4/5.0 versus 4.0/5.0 for SPECT/CT. Importantly, as a result of these findings, the FDA agreed to the following important modifications to the Phase 3 protocol:

(1) All certified SPECT/CT systems used in the Phase 3 study must have a CT that provides an AC reconstruction slice thickness of 5 mm or better.

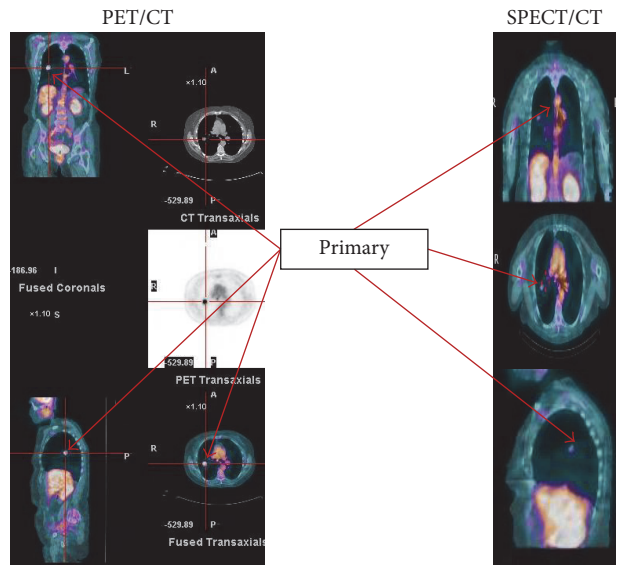

Figure 5: Comparative SPECT/CT: ^{99m}Tc- EC-G and PET/CT: ^{18}F-FDG image sets on a 68-year-old patient having a biopsy confirmed primary NSCLC.

(2) All suspicious lesions identified by the SPECT and/or PET core laboratory readers must be confirmed by either a tissue diagnosis or evidence for contrast enhancement from a baseline diagnostic CT contrast (DCCT) study to eliminate the possibility of a false positive interpretation for ^{18}F-FDG due to uptake in infection or inflammation.

Example of image sets showing detection of primary tumors and metastasis for ^{18}F-FDG PET/CT and ^{99m}Tc-EC-G SPECT/CT is shown in Figures 5–7. In all cases the slice thickness for the reconstructed AC maps is 5 mm or better.

5. Discussion

The Phase 2 studies completed on 17 patients expanded the patient safety experience using ^{99m}Tc-EC-G and provided evidence of ^{99m}Tc-EC-G imaging efficacy in identifying anatomical regions with known non-small cell lung cancer and in determining the extent of disease (metastasis) in these patients as noninferior to ^{18}F-FDG PET/CT imaging. Specifically, the Phase 2 study demonstrated equivalent detection (100%) of primary lesions (biopsied) by SPECT/CT and PET/CT (sensitivity only) and noninferiority to detectability (70% agreement) for metastatic lesions between SPECT/CT and PET/CT.

In addition, the Phase 2 study showed that ^{99m}Tc-EC-G SPECT/CT imaging has the potential to serve as an alternative to ^{18}F-FDG PET/CT imaging for diagnosing and staging oncology patients. In particular, the Phase 2 study provided equivalent diagnostic information with good accumulation in lung cancer and associated metastatic lesions using gamma cameras from three device manufacturers (Philips Healthcare, Siemens Healthcare, and GE Healthcare) as well as for a Philips SPECT system integrated to a Philips CT system

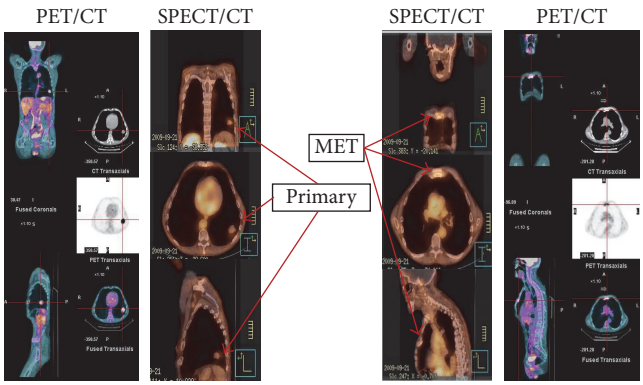

Figure 6: Comparative SPECT/CT: ^{99m}Tc- EC-G and PET/CT: ^{18}F-FDG image sets on a 56-year-old patient having a biopsy confirmed primary NSCLC and diagnostic CT contrast confirmed metastasis to the sternum.

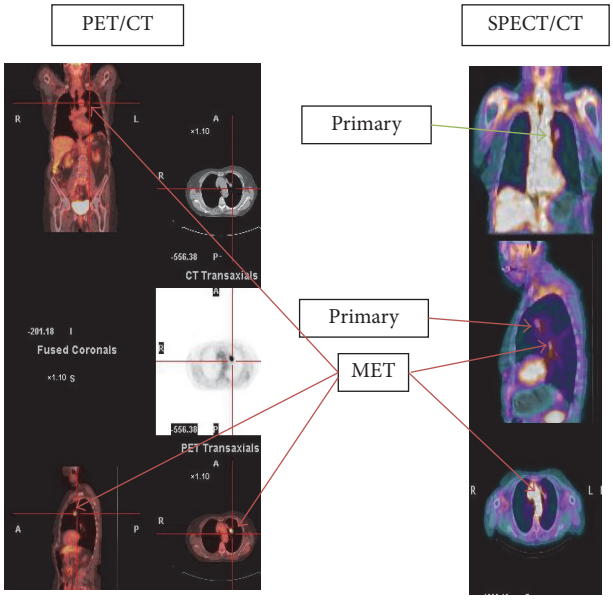

Figure 7: Comparative SPECT/CT: ^{99m}Tc- EC-G and PET/CT: ^{18}F-FDG image sets on a 61-year-old patient having a biopsy confirmed primary NSCLC and diagnostic CT contrast confirmed metastasis to the lung.

via a Philips work station, provided the imaging device has a CT with 5 mm or better slice thickness for reconstructing AC maps and image fusion. The Phase 2 study also showed that when the specific activity of ^{99m}Tc-EC-G was increased from 5 mg of EC-G labeled with 925 BCq of ^{99m}Tc to 1 mg of EC-G labeled with 925 BCq of ^{99m}Tc, the tumor/background ratio for both the primary and metastatic lesions improved significantly. It was also shown that when the time to image was changed from 2 to 3 hours after injection, there was additional improvement in the tumor/background ratio. Thus, the Phase 3 study design requires specific characteristics for SPECT/CT technology, high specific activity for ^{99m}Tc-EC-G, and a 3-hour postinjection imaging time to assure the highest detectability of small lesions even in the presence of dense tissue.

An extremely important issue identified in Phase 2 relates to whether lesions detected by either SPECT or PET that do not have a tissue diagnosis are in fact malignant. For example, it is now known that 18F-FDG localizes in infection and inflammation as well as malignant tumors. The results of the Phase 2 study and the Study Design, Protocol and Statistical Analysis Plan for the pivotal Phase 3 study were presented to the FDA. The FDA granted the proposed Phase 3 study with a Special Protocol Assessment Letter of Agreement.

A summary of the main features of the Phase 3 study includes the following:

(1) The Phase 3 study was designed for noninferiority. Hypothesis testing of the results of the Phase 2 primary endpoint of sensitivity for detection of the biopsied primary lesion combined with the objective measure for detecting metastasis resulted in the following parameters being accepted by the FDA:

(i) An estimated 165–190 patients, for each of the two identical clinical arms

(ii) A margin of 10% between SPECT/CT: 99mTc-EC-G and PET/CT: 18F–FDG

(iii) A required confidence interval of 95%.

(2) The patient population was expanded to include all lung cancer types.

(3) Criteria for patient enrollment include any patient with clinical and radiological evidence consistent with lung cancer that has been referred for a PET scan to confirm the diagnosis and/or for staging the disease.

(4) All patients enrolled must agree to a tissue diagnosis of the primary lesion; a baseline diagnostic CT with contrast study; and a whole-body bone scan independent of the results of the PET/CT study.

(5) The Phase 3 study Truth Standard will be tissue diagnosis (primary as well as metastatic lesions when available) or evidence for contrast enhancement/or not from the diagnostic CT with contrast scan on suspicious lesions.

(6) The blinded read imaging interpretation by the Core Lab readers for the presence of malignancy for both PET and SPECT will be compared against the Truth Standard for every detectable lesion.

For this reason, Phase 3 will require that all suspicious lesions detected by either radiopharmaceutical compound be validated for malignancy. This will include a requirement that all primary lesions have a tissue diagnosis. In addition, a tissue diagnosis (open or closed biopsy) is performed whenever possible or practical in respect to any suspicious metastatic lesions. Suspicious metastatic lesions that do not have tissue confirmation will be deemed malignant if the baseline Standard of Care DCCT scan consensus interpretation by 2 independent truth standard core laboratory readers (readers who are independent/different from the core laboratory PET and SPECT readers) determines the lesions(s) to have vascular and anatomical patterns (contrast enhancement) consistent with malignancy. Phase 3 trial would categorize the patients into clinically statistical relevant groups such as percent of

patients of NSCLC highlighting the need of 99mTc-EC-G for diagnostic tests to identify the subpopulations of patients who will benefit from this diagnostic/therapeutic trial.

6. Conclusions

^{99m}Tc-EC-G was well tolerated. All but 2 AEs (nausea and vomiting, considered mild and unlikely related to the study drug) were considered unrelated to study drug. There were 6 SAEs, all considered unrelated to the study drug, and there were no deaths or AEs leading to withdrawal. No clinically significant trends or abnormalities were observed in vital sign measurements or EKGs.

The ^{99m}Tc-EC-G SPECT/CT results compared to the ^{18}F-FDG PET/CT results showed 100% agreement for detection of primary lesions, determination of location and lesion size, and confidence that the detected lesion represented a malignancy. Detection of primary lesions was not influenced by the dose of ^{99m}Tc-EC-G or by the time of imaging in the range of doses and times used in the study. Detection of primary lesion was also not influenced by the type of imaging device or the device vendor. Overall, the study results demonstrated noninferiority in detecting primary lesions (biopsied) of ^{99m}Tc-EC-G SPECT/CT compared to ^{18}F-FDG PET/CT (sensitivity only). Metastatic lesions were shown to localize EC-G for both the 1 and 5 mg dose of EC-G, but the detectability of lesions by SPECT/CT was at a lower level than that noted for PET/CT when the CT slice thickness for reconstruction of AC maps and image fusion was 1 cm. Despite this issue, the overall detectability, lesion location and size, and confidence that a suspicious lesion was malignant showed overall noninferiority to the same measures reported for ^{18}F-FDG PET/CT (4.4/5.0 versus 4.0/5.0), respectively. The results of the Phase 2 study were warranted for the pivotal Phase 3 study.

Disclosure

F. David Rollo is the co-first author.

Conflicts of Interest

The authors declare that they have no conflicts of interest.

Acknowledgments

The EC-Technology was licensed from the University of Texas MD Anderson (Houston, TX) to Cell➤Point, LLC (Centennial, CO). This work was supported by the Cell➤Point, LLC. The authors wish to thank for helpful feedback and discussions from the clinic trial sites. This work was supported in part by grants from the National Natural Science Foundation of China (Grant no. 81601377) and Tianjin Natural Science Fund (16JCZDJC35200, 17JCYBJC25100). The authors especially thank Dr. David J. Yang for his contribution in providing the mechanism of action and preclinic findings of EC-G.

References

[1] L. Andresen, S. L. Skovbakke, G. Persson et al., "2-deoxy D-glucose prevents cell surface expression of NKG2D ligands through inhibition of N-linked glycosylation," *The Journal of Immunology*, vol. 188, no. 4, pp. 1847–1855, 2012.

[2] A. Buerkle and W. A. Weber, "Imaging of tumor glucose utilization with positron emission tomography," *Cancer and Metastasis Reviews*, vol. 27, no. 4, pp. 545–554, 2008.

[3] R. Boellaard, R. Delgado-Bolton, W. J. G. Oyen et al., "FDG PET/CT: EANM procedure guidelines for tumour imaging: version 2.0," *European Journal of Nuclear Medicine and Molecular Imaging*, vol. 42, no. 2, pp. 328–354, 2014.

[4] K. E. Wellen, C. Lu, A. Mancuso et al., "The hexosamine biosynthetic pathway couples growth factor-induced glutamine uptake to glucose metabolism," *Genes & Development*, vol. 24, no. 24, pp. 2784–2799, 2010.

[5] K. Shirato, K. Nakajima, H. Korekane et al., "Hypoxic regulation of glycosylation via the N-acetylglucosamine cycle," *Journal of Clinical Biochemistry and Nutrition*, vol. 48, no. 1, pp. 20–25, 2011.

[6] S. P. N. Iyer and G. W. Hart, "Dynamic nuclear and cytoplasmic glycosylation: Enzymes of O-GlcNAc cycling," *Biochemistry*, vol. 42, no. 9, pp. 2493–2499, 2003.

[7] A. J. Paterson and J. E. Kudlow, "Regulation of glutamine:fructose-6-phosphate amidotransferase gene transcription by epidermal growth factor and glucose," *Endocrinology*, vol. 136, no. 7, pp. 2809–2816, 1995.

[8] S. Marshall, V. Bacote, and R. R. Traxinger, "Discovery of a metabolic pathway mediating glucose-induced desensitization of the glucose transport system: role of hexosamine biosynthesis in the induction of insulin resistance," *The Journal of Biological Chemistry*, vol. 266, no. 8, pp. 4706–4712, 1991.

[9] L. Wells, Y. Gao, J. A. Mahoney, K. Vosseller, A. Rosen, and G. W. Hart, "Dynamic O-glycosylation of nuclear and cytosolic proteins: Further characterization of the nucleocytoplasmic β-N-acetylglucosaminidase, O-GlcNAcase," *The Journal of Biological Chemistry*, vol. 277, no. 3, pp. 1755–1761, 2002.

[10] L. Wells, K. Vosseller, and G. W. Hart, "Glycosylation of nucleocytoplasmic proteins: signal transduction and O-GlcNAc," *Science*, vol. 291, no. 5512, pp. 2376–2378, 2001.

[11] G. W. Hart, C. Slawson, G. Ramirez-Correa, and O. Lagerlof, "Cross talk between O-GlcNAcylation and phosphorylation: roles in signaling, transcription, and chronic disease," *Annual Review of Biochemistry*, vol. 80, pp. 825–858, 2011.

[12] T. P. Lynch, C. M. Ferrer, S. R. Jackson, K. S. Shahriari, K. Vosseller, and M. J. Reginato, "Critical role of O-linked β-N-acetylglucosamine transferase in prostate cancer invasion, angiogenesis, and metastasis," *The Journal of Biological Chemistry*, vol. 287, no. 14, pp. 11070–11081, 2012.

[13] U. Hummel, C. Nuoffer, B. Zanolari, and B. Erni, "A functional protein hybrid between the glucose transporter and the N-acetylglucosamine transporter of Escherichia coli," *Protein Science*, vol. 1, no. 3, pp. 356–362, 1992.

[14] D. Maszczak-Seneczko, P. Sosicka, T. Olczak, P. Jakimowicz, M. Majkowski, and M. Olczak, "UDP-N-acetylglucosamine transporter (SLC35A3) regulates biosynthesis of highly branched N-glycans and keratan sulfate," *The Journal of Biological Chemistry*, vol. 288, no. 30, pp. 21850–21860, 2013.

[15] D. J. Yang, C.-G. Kim, N. R. Schechter et al., "Imaging with 99mTc ECDG targeted at the multifunctional glucose transport

system: Feasibility study with rodents," *Radiology*, vol. 226, no. 2, pp. 465–473, 2003.

[16] D. Yang, M. Yukihiro, D.-F. Yu et al., "Assessment of therapeutic himor response using 99mTc- ethylenedicysteine-glucosamine," *Cancer Biotherapy and Radiopharmaceuticals*, vol. 19, no. 4, pp. 443–456, 2004.

[17] N. R. Schechter, W. D. Erwin, D. J. Yang et al., "Radiation dosimetry and biodistribution of 99mTc-ethylene dicysteine-deoxyglucose in patients with non-small-cell lung cancer," *European Journal of Nuclear Medicine and Molecular Imaging*, vol. 36, no. 10, pp. 1583–1591, 2009.

[18] Y.-H. Zhang, J. Bryant, F.-L. Kong et al., "Molecular imaging of mesothelioma with 99mTc-ECG and 68Ga-ECG," *Journal of Biomedicine and Biotechnology*, vol. 2012, Article ID 232863, 9 pages, 2012.

[19] T. Inoue, D. Yang, and G. Huang, *Personalized Pathway-Activated Systems Imaging in Oncology*, Springer Singapore, Singapore, 2017.

[20] D. J. Yang, F.-L. Kong, T. Oka, and J. L. Bryant, "Molecular imaging kits for hexosamine biosynthetic pathway in oncology," *Current Medicinal Chemistry*, vol. 19, no. 20, pp. 3310–3314, 2012.

[21] L. V. Pham, J. L. Bryant, R. Mendez et al., "Targeting the hexosamine biosynthetic pathway and O-linked N-acetylglucosamine cycling for therapeutic and imaging capabilities in diffuse large B-cell lymphoma," *Oncotarget*, vol. 7, no. 49, pp. 80599–80611, 2016.

Hindawi
Contrast Media & Molecular Imaging
Volume 2017, Article ID 8598705, 7 pages
https://doi.org/10.1155/2017/8598705

Research Article

F-18 FP-CIT PET in Multiple System Atrophy of the Cerebellar Type: Additional Role in Treatment

Young Jin Jeong,[1,2] Sang-Myung Cheon,[3] Do-Young Kang,[1,2] and Jae Woo Kim[3]

[1]*Department of Nuclear Medicine, Dong-A University Hospital, Dong-A University College of Medicine, Busan, Republic of Korea*
[2]*Institute of Convergence Bio-Health, Dong-A University, Busan, Republic of Korea*
[3]*Department of Neurology, Dong-A University Hospital, Dong-A University College of Medicine, Busan, Republic of Korea*

Correspondence should be addressed to Sang-Myung Cheon; smcheon@dau.ac.kr

Received 16 October 2017; Accepted 14 November 2017; Published 29 November 2017

Academic Editor: Paulo H. Rosado-de-Castro

We evaluated the difference in the status of dopamine transporters (DATs) depending on Parkinsonism, cerebellar, and autonomic features using F-18 FP-CIT positron emission tomography (PET) in multiple system atrophy with cerebellar ataxia (MSA-C). We also assessed whether the DAT PET could be useful in the management of MSA-C. Forty-nine patients who were clinically diagnosed as possible to probable MSA-C were included. Based on the F-18 FP-CIT PET results, patients were classified into normal ($n = 25$) and abnormal ($n = 24$) scan groups. There were statistically significant differences in rigidity, bradykinesia, postural instability, asymmetry, and specific uptake ratio (SUR) between the two groups but no significant differences in tremor and cerebellar/autonomic symptoms. Dopaminergic medications were administered to 22 patients. All seven patients with normal scans showed no change, while 10 of the 15 patients with abnormal scans showed clinical improvement. There was a trend of a negative correlation between levodopa equivalent dose and SUR, but it was not statistically significant. DAT imaging, such as F-18 FP-CIT PET, may be useful in predicting the response to dopaminergic medication regardless of cerebellar/autonomic symptoms in MSA-C. In addition to being used for the diagnosis of the disease, it may be used as a treatment decision index.

1. Introduction

Multiple system atrophy (MSA) is an adult-onset, sporadic neurodegenerative disorder pathologically characterized by prominent alpha-synuclein (a-Syn) inclusions with neuronal degeneration. Clinically, cardinal features of the disorder are Parkinsonism, cerebellar ataxia, autonomic failure, and corticospinal tract dysfunction. There are two clinical subtypes depending on the predominant motor presentation: a Parkinsonian variant reflecting underlying nigrostriatal degeneration (MSA-P) and a cerebellar variant associated with cerebellar ataxia (MSA-C) [1].

Although cerebellar symptoms are a major feature of MSA-C, Parkinsonian features are also observed [2]. This is supported by a pathologic study that revealed that a-Syn involvement and neuronal loss occurred not only in the cerebellum, pons, and olives but also in the striatum in MSA-C [3]. This nigrostriatal degeneration of MSA-C can also be visualized in imaging studies; it has been reported that striatal dopamine transporter (DAT) is reduced to various degrees in DAT imaging, such as F-18 fluorinated-N-3-fluoropropyl-2-b-carboxymethoxy-3-b-(4-iodophenyl)nortropane (FP-CIT) positron emission tomography (PET) [4–7]. F-18 FP-CIT PET can be used to assess dopaminergic neuronal degeneration by evaluating the density of DATs. Because many motor disorders characterized by Parkinsonian features exhibit various degrees of degeneration of dopaminergic neurons, DAT imaging, such as F-18 FP-CIT PET, is currently being used clinically for the evaluation of these diseases [5, 6]. In MSA, F-18 FP-CIT PET is mainly investigated in MSA-P, in which nigrostriatal symptoms are predominant, and it is relatively less studied in MSA-C. As seen in the MSA-C diagnostic guideline [1], there have been many studies on the use of perfusion single photon emission computed tomography or F-18 fluorodeoxyglucose (FDG) PET in the diagnosis of the disease by evaluating the decrease in blood flow or glucose metabolism in the cerebellum or striatum [8–12]. In the F-18 FP-CIT PET studies, various levels of striatal dopamine

receptors have been reported [4–7], but the usefulness of the PET scan in disease evaluation has not yet been established in MSA-C.

Clinically, there is no cure for MSA, and management of MSA in focused on symptomatic relief [13]. Parkinsonism, cerebellar, and autonomic symptoms should be treated judiciously [2]. Dopaminergic medications for the treatment of Parkinsonism can often induce dyskinesia or aggravate autonomic symptoms, especially orthostatic hypotension [2]. This sometimes makes it difficult for neurologists to decide on medicines for Parkinsonism, but there are no indicators to support the determination of drug administration other than clinical judgments based on neurological examinations. In particular, cerebellar ataxia of MSA-C can make it hard for clinicians to evaluate Parkinsonism. Therefore, objective indicators of the status of Parkinsonism may help them make treatment decisions. Previous studies on idiopathic Parkinson's disease (IPD) have commonly reported that the DAT status of F-18 FP-CIT PET is associated with the degree of Parkinsonian symptoms [14–17]. Likewise, in MSA-C, F-18 FP-CIT PET can show the status of the presynaptic dopaminergic function, so it can be considered a marker of Parkinsonism in MSA-C. If so, F-18 FP-CIT PET may be helpful in the treatment as well as diagnosis of MSA-C.

In the present study, we evaluated the difference in the status of DAT depending on Parkinsonism, cerebellar, and autonomic features and assessed whether F-18 FP-CIT PET could be useful in the treatment of Parkinsonism in MSA-C.

2. Materials and Methods

2.1. Patients. Forty-nine patients with clinically possible or probable MSA-C (M : F = 30 : 19, 61.6 ± 6.5 yrs) were retrospectively enrolled in this study. Clinically, 21 patients had possible MSA-C (M : F = 13 : 8, 59.7 ± 6.3 yrs), and 28 patients had probable MSA-C (M : F = 17 : 11, 62.9 ± 6.4 yrs). The diagnosis of MSA-C was done by movement disorder specialists based on the current diagnostic criteria in patients with adult-onset (older than age of 40) progressive ataxia who had no relevant family history and no established acquired etiology of ataxia [1, 17]. All medical records were available, and the neurologists checked for motor disability, such as Parkinsonism (e.g., tremor, rigidity, bradykinesia, and postural instability), cerebellar features (e.g., gait ataxia, limb ataxia, cerebellar dysarthria, and cerebellar oculomotor dysfunction), and autonomic symptoms (e.g., orthostatic hypotension, urinary incontinence, and erectile dysfunction). The neurologists defined Parkinsonism as having definite bradykinesia and rigidity.

In patients taking dopaminergic medication for the treatment of Parkinsonism, doses of the drugs were investigated and expressed as levodopa equivalent doses (LEDs) [18]. Movement disorder specialists assessed the response to dopaminergic medication based on the clinical rating if there was a clinically meaningful improvement. Patients who took the medication for less than 3 months, discontinued the medication due to side effects, or were unable to confirm the response were excluded from the analysis.

Patients with Parkinson's disease, other atypical or secondary Parkinsonism, head trauma, stroke, dementia, or psychological disorders were excluded. In our normal database of F-18 FP-CIT PET, 10 healthy individuals who did not have any clinical symptoms related to Parkinsonism were selected. The Institutional Review Board of our hospital reviewed and approved the study protocol and informed consent form.

2.2. F-18 FP-CIT PET/CT and Image Analysis. All the F-18 FP-CIT PET/CT examinations were performed using a Discovery 710 PET/CT (GE Healthcare, Milwaukee, WI, USA) scanner. Patients were intravenously injected with 185 MBq F-18 FP-CIT and PET/CT acquisition was started 180 min after the radiotracer injection. F-18 FP-CIT was supplied by FutureChem in Republic of Korea. A helical CT scan was carried out with a rotation time of 0.5 s at 120 kVp and 100 mAs without an intravenous contrast agent. A PET scan followed immediately and was acquired for 10 min in the three-dimensional mode. All the images were acquired from the skull vertex to the skull base. The patients were allowed to continue their anti-Parkinson medication.

Two experienced nuclear medicine physicians reviewed all the PET/CT images using a dedicated workstation with custom software (Advantage Workstation 5.0). The striatal volumetric analysis was done following a previous study [19]. To analyze the striatal functional volume, a semiautomatically delineated spherical volume-of-interest (VOI) was drawn over each of the two strata (Figure 1). The striatal target volume was segmented with custom software using a gradient-based method that detected the striatal margin based on a change in activity levels near the structure margin automatically [20]. We drew the VOI over the occipital lobe, and the value of the functional striatal volume multiplied by the occipital mean standardized uptake value (SUV mean) was considered nonspecific uptake of the striatum. Specific uptake ratios (SURs) were calculated for the target striatal VOI, and these values were defined as follows: mean standardized uptake value (mean SUV) of striatal VOI − mean SUV of occipital VOI/mean SUV of occipital VOI.

F-18 FP-CIT PET images were classified into normal and abnormal scans by visual and quantification analysis. First, the visual assessment was done using the morphology and density of the striatum and striatal asymmetry. Second, quantification analysis was performed based on the values of healthy subjects. The SUR cut-off value in the healthy subjects was 2.84. If the visual and quantification analyses showed the same results, the scan results were classified accordingly, while discordant cases were categorized by the agreement of two nuclear medicine physicians.

2.3. Statistical Analysis. The differences in patient characteristics and clinical symptoms between the normal and abnormal scan groups of F-18 FP-CIT PET were evaluated using the Mann–Whitney U test for continuous variables and the Chi-square test or Fisher's exact test for categorical variables. Fisher's exact test was performed to evaluate the response to dopaminergic medication according to the scan result. The relation between LED and various parameters was evaluated using Spearman's rho. Statistical analyses were

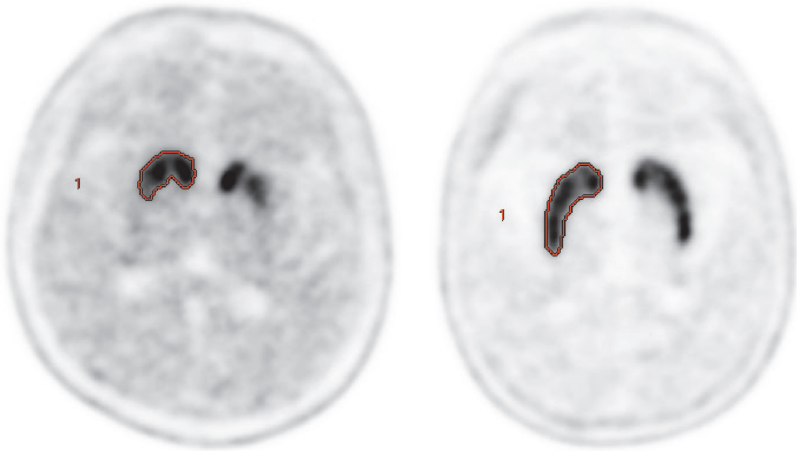

(a) (b)

Figure 1: F-18 FP-CIT images of normal scan (a) and abnormal scan (b) groups. The gradient-based VOIs were automatically drawn on the striatum in the PET images.

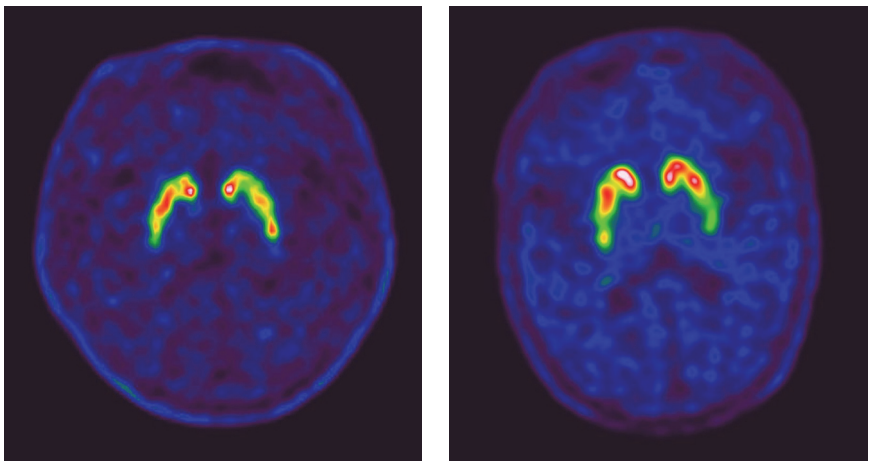

(a) (b)

Figure 2: Two patients were normal in the quantitative analysis but abnormal in the visual assessment. One patient showed very heterogeneous uptake in both strata (a), and the other patient showed significantly decreased uptake in the tail portion of both putamens (b).

performed using MedCalc software version 16.4 (MedCalc Software, Mariakerke, Belgium). Statistical significance was defined as p value < 0.05.

3. Results

3.1. Patients Characteristics and Difference between Normal and Abnormal Scan Groups (Table 1). In F-18 FP-CIT PET, of all 49 MSA-C patients, 47 showed consistent findings in the visual and quantification analyses. Twenty-five patients were normal, and 22 were abnormal in both analyses consistently. The other two patients showed discordant results, which were quantitatively normal but visually abnormal. After checking again, one patient showed very heterogeneous uptake in both strata, and the other patient showed significantly decreased uptake in the tail portion of both putamens (Figure 2). Therefore, these two patients were placed in the abnormal scan group despite their normal quantification results. Finally, 25 (51.0%) patients were in the normal scan group, and 24 (49.0%) patients were in the abnormal scan group. There were no differences in age, sex, or disease duration between the two groups. Clinically confirmed Parkinsonism was more frequent in the abnormal scan group (32.0% versus 66.7%, $p = 0.0163$). Among Parkinsonian features, rigidity ($p = 0.0004$), bradykinesia ($p = 0.0082$), and postural instability ($p = 0.0040$) were significantly more common in the abnormal scan group than the normal scan group, but there was no significant difference in resting tremor ($p = 0.3209$). There was no significant difference between the two groups in the frequency of cerebellar features, such as gait ataxia

Table 1: Difference in characteristics of the patients between normal and abnormal scan groups.

Characteristics	Normal scan (n = 25)	Abnormal scan (n = 24)	p value[1]
Age (years)	61.7 ± 6.6	61.5 ± 6.5	0.9272
Sex (male : female)	18 : 7	12 : 12	0.0939
Disease duration (years)	3.1 ± 1.5	3.0 ± 1.6	0.8441
Parkinsonism	8 (32.0%)	16 (66.7%)	***0.0163***
Bradykinesia	14 (56.0%)	22 (91.7%)	***0.0082***
Bradykinesia (score)	1.0 ± 0.9	1.6 ± 0.8	***0.0142***
Rigidity	8 (32.0%)	20 (83.3%)	***0.0004***
Rigidity (score)	0.3 ± 0.5	0.9 ± 0.5	***0.0003***
Postural instability	17 (68.0%)	24 (100.0%)	***0.0040***
Resting tremor	4 (16.0%)	7 (29.2%)	0.3209
Cerebellar symptom			
Gait ataxia	25 (100.0%)	24 (100.0%)	1.0000
Limb ataxia	22 (88.0%)	22 (91.7%)	1.0000
Cerebellar dysarthria	22 (88.0%)	23 (95.8%)	1.0000
Oculomotor dysfunction	18 (72.0%)	22 (91.7%)	0.1383
Autonomic symptom			
Orthostatic hypotension	12 (48.0%)	9 (36.0%)	0.4624
Urinary incontinence	10 (40.0%)	13 (54.2%)	0.3255
Erectile dysfunction	10/18 (55.6%)	9/12 (75.0%)	0.4425
PET parameter			
Striatal asymmetry	0.97 ± 0.03	0.88 ± 0.10	***0.0006***
Striatal SUR	3.98 ± 0.58	2.59 ± 0.89	***<0.0001***

[1] p value in bold, italic type indicates statistical significance. SUR: specific uptake ratio.

(p = 1.0000), limb ataxia (p = 1.0000), cerebellar dysarthria (p = 1.0000), and cerebellar oculomotor dysfunction (p = 0.1383). There was also no significant difference between the two groups in the frequency of autonomic symptoms, such as orthostatic hypotension (p = 0.4624), urinary incontinence (p = 0.3255), and erectile dysfunction (p = 0.4425). In F-18 FP-CIT PET, the abnormal scan group showed significant asymmetry in the striatum (0.97 versus 0.88, p = 0.0006). SUR was also significantly lower in the abnormal scan group (3.98 versus 2.59, p < 0.0001).

3.2. Treatment Response of Dopaminergic Medication of Normal and Abnormal Scan Groups. Of the 49 patients, 39 had taken dopaminergic medication, including levodopa and dopamine agonists, according to the clinical judgment of neurologists, but 17 of these patients were excluded in the response analysis for the reasons mentioned above. Of the patients taking the drug, the remaining 22 patients were included in the analysis. Of the 22 patients taking medication, seven patients showed normal striatal uptake and 15 patients showed decreased striatal uptake in F-18 FP-CIT PET. After the chronic administration of dopaminergic medication (1.7 ± 0.9 years, 464 ± 200 mg/day in LED), 10 of 22 patients showed clinical improvement (45.5%). There was no response in all seven patients with normal striatal uptake. Ten of the 15 patients (66.7%) with abnormal striatal uptake showed a response to the medication (Figure 3). Fisher's exact test revealed a significant difference in the response rate between the normal and abnormal scan groups (p = 0.005).

3.3. Relationship between Dopaminergic Medication Dose and Striatal Uptake of F-18 FP-CIT PET. The mean LED was 464 ± 200 mg/day in the 22 patients who received dopaminergic medication. The mean LED was 386 ± 180 mg/day in the 12 patients who had no response to the drug and 488 ± 205 mg/day in the 10 patients who had a response to the drug, and there was no significant difference in the LED between the two groups (p = 0.2823). We examined the relationship of LED with the grade of bradykinesia, rigidity, and SUR in the 10 patients who were clinically responsive among the 22 patients who received dopaminergic medication. LED was not significantly correlated with grade of bradykinesia (r = −0.450, 95% confidence interval (CI) = −0.205–0.827, p = 0.1648) or rigidity (r = −0.426, 95% CI = −0.817–0.234, p = 0.1915). There was trend of a negative correlation between LED and SUR, but it was not statistically significant (r = −0.456, 95% CI = −0.844–0.243, p = 0.1848, Figure 4).

4. Discussion

In MSA, F-18 FP-CIT PET is widely used clinically for disease evaluation of MSA-P, because it represents the characteristic

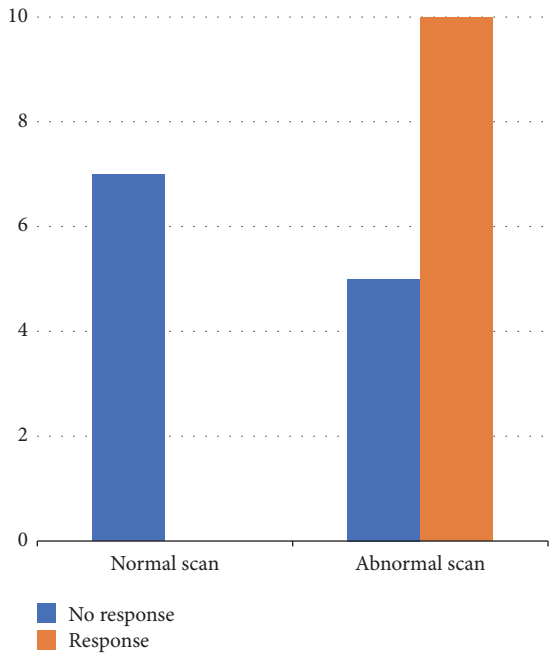

Figure 3: Bar chart showing responsiveness to dopaminergic medication in normal and abnormal scan groups. There was no response in all patients with normal scans and some response in the abnormal scan group.

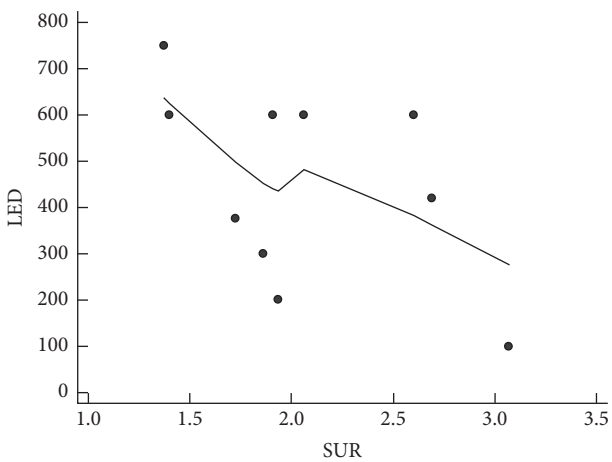

Figure 4: Correlation analysis between levodopa equivalent dose (LED) and specific uptake ratio (SUR) showing a trend of a negative, but not statistically significant, relationship ($r = -0.456$, $p = 0.1848$).

degeneration of presynaptic nigrostriatal dopaminergic nerves as in IPD. The clinical significance of F-18 FP-CIT PET has not yet been clearly established in MSA-C, but several studies have reported varying degrees of striatal uptake [4–7]. In the present study, of 49 patients, 25 (51.0%) were normal and 24 (49%) were abnormal in F-18 FP-CIT PET. The mean decline of SUR in the striatum was about 35% of that in normal subjects. Previous studies reported similar results of a reduction range between 21% and 79% [4, 7, 21]. Although it is generally known that nigrostriatal dopaminergic neurons are relatively uniformly reduced in MSA, the abnormal scan group of MSA-C in this study was asymmetrically reduced compared to normal subjects. These findings correlate well with a pathologic study indicating that neuronal loss of the nigrostriatal tract was heterogeneous according to the disease status [3], and a German multicenter study also reported that approximately 50% of MSA patients of their cohort revealed asymmetry of clinical symptoms [22]. Our results showed that striatal uptake of F-18 FP-CIT PET clearly reflected clinical Parkinsonian symptoms in MSA-C. Among the Parkinsonian features, the frequency of rigidity, bradykinesia, and postural instability and the severity of rigidity and bradykinesia were significantly higher in the abnormal scan group compared with the normal scan group. Resting tremor was not different between the two groups; this result could be explained by the fact that resting tremor is not directly related to the loss of nigral dopaminergic neurons [16]. This result was similar to those of previous studies on IPD [14–18]. Based on these results, F-18 FP-CIT PET also represents the nigrostriatal dopaminergic neuronal degeneration in MSA-C as in IPD.

However, in order for F-18 FP-CIT PET to have a significant clinical role in MSA-C, the results of the study should not be affected by motor dysfunction due to cerebellar or autonomic dysfunction. Our study showed that regardless of the F-18 FP-CIT PET results, most patients had cerebellar dysfunction and there was no significant difference in cerebellar or autonomic symptoms between the normal and abnormal scan groups. These results suggest that nigrostriatal neuronal degeneration occurs independently from cerebellar and autonomic neuronal degeneration. A previous study reported similar results, which showed no correlation between striatal uptake in DAT SPECT and clinical cerebellar disability [21]. Pathologic studies supporting these results indicated that region-specific cell loss was reported in MSA [3, 23, 24]. In particular, in MSA-C, neuronal loss predominantly involves the olivopontocerebellar structure and frequently the nigrostriatal tract and autonomic nuclei [3, 13]. However, region-specific neuronal degeneration occurs independently [23, 24]. Therefore, F-18 FP-CIT can demonstrate the status of presynaptic nigrostriatal dopaminergic degeneration regardless of cerebellar or autonomic dysfunction.

One of the purposes of the present study was to determine whether F-18 FP-CIT PET has a role in the treatment of Parkinsonism in MSA-C. Currently, symptomatic treatment is only available for MSA-C, and the two main targets of symptomatic treatment are Parkinsonism and autonomic dysfunction [2, 13]. Although the response to dopaminergic medication is poor or transient, about half of patients with MSA-C respond to the medication [2]. To evaluate drug responsiveness, the dopaminergic medications should be given for 3 months at an escalating dose, but orthostatic hypotension can be aggravated by the medication and about half of the patients with drug treatment show dyskinesia [2, 13, 22]. These problems make neurologists hesitant to prescribe medication; thus, they need an indicator that can help them decide whether to prescribe the medicine. In this

study, through a chart review by a neurologist, we evaluated 22 patients' responsiveness to dopaminergic medications. All seven patients (100%) with normal scans showed no clinical response, and 10 of the 15 patients (66.7%) with abnormal scans showed a clinical response to the medication. Normal findings in F-18 FP-CIT PET suggested no nigrostriatal denervation. Therefore, the drug seemed to have no effect on all seven patients in the normal group. Clinically, even if a suspicion of Parkinsonism in MSA-C patients may be normal in F-18 FP-CIT PET, this discrepancy could be explained by the difficulty of diagnosis due to the manifestation of various motor function abnormalities in MSA-C. In the 15 patients who showed abnormal PET scans, 10 patients had a response to the drug, but one-third of the patients had no response. We could not find any difference in clinical and imaging characteristics between the two groups of patients (data not shown). Pathologic and imaging studies have demonstrated that postsynaptic dopamine D2/3 receptor and presynaptic DAT are also decreased in MSA [3, 25, 26]. Because dopamine D2/3 receptor provides inhibitory motor control, the reduction of the receptor leads to a loss of motor control. Since the motor dysfunction in MSA-C is due to the combined effect of pre- and postsynaptic receptors of the dopaminergic nerve, it is difficult to correctly assess the degeneration of dopaminergic neurons with only the F-18 FP-CIT PET showing only presynaptic DAT. In the presence of severe dopamine D2/3 receptor decline, an effect of the dopaminergic drug is unlikely. In this study, the five patients with no response to the drug of the 15 patients with abnormal scans would be considered in this case, but accurate evaluation requires additional dopamine D2/3 receptor imaging. Based on these results, it can be suggested that if F-18 FP-CIT PET shows normal findings in MSA-C patients, it may not be necessary to administer dopaminergic medications because drug effects are unlikely. In addition, in patients with abnormal PET findings, dopaminergic medication may be considered.

We thought that the degree of DAT reduction in F-18 FP-CIT might be correlated with the need for the drug. Nissen et al. reported that although the correlation was not strong, the amount of dopaminergic drug required increased significantly with decreasing DAT uptake ($r = -0.26$, $p = 0.0201$) [27]. In this study, a trend of an inverse association between LED and SUR was shown, but it was not statistically significant ($r = -0.456$, $p = 0.1848$). The possible explanation was that, as mentioned above, the state of the nigrostriatal dopaminergic pathway was not completely evaluated in F-18 FP-CIT PET showing only the presynaptic DAT state. In addition, the neurologist considered the adverse effect of the drug and adjusted the dose according to the patient's response. However, there was a trend of a negative relationship. Thus, a further study with a large population is needed.

The present study had some limitations. We could not investigate responsiveness to dopaminergic medication quantitatively, because this study was performed retrospectively based on a chart review. In addition, for the analysis of the response to dopaminergic medication, we included only those patients whose drug effects were clearly marked on the chart as a result of clinical judgments by movement disorder specialists. Moreover, we did not consider the normal aging effect in the quantification analysis of F-18 FP-CIT PET. Previous studies reported that DAT ligand (e.g., FP-CIT) binding in the normal striatum decreased with age at a rate of 5.3–7.7% per decade [28, 29]. Therefore, age correction is recommended for accurate quantification. In this study, except for four patients in their 70s, all patients were in their 50s and 60s. Most of the normal controls were also in their 50s and 60s. Thus, we thought the aging effect on the quantification results of F-18 FP-CIT PET would not be significant. Finally, misdiagnosis of clinically probable or possible MSA-C could be possible because no post-mortem confirmation was available. However, the diagnostic criteria for MSA have a high diagnostic accuracy [30]. Also, the mean disease duration of the patients was about 3 years, and patients with other cerebellar and Parkinsonism-related disease were excluded from this study.

In conclusion, this study suggests that F-18 FP-CIT PET imaging may be useful in predicting the effect of dopaminergic medication regardless of cerebellar or autonomic symptoms in MSA-C. In addition to being used for the diagnosis of the disease, F-18 FP-CIT PET may be used as a treatment decision index.

Conflicts of Interest

The authors declare that they have no conflicts of interest.

Acknowledgments

This work was supported by the Busan Metropolitan City research fund.

References

[1] G. Wenning, S. Gilman, and K. Seppi, "Second consensus statement on the diagnosis of multiple system atrophy," *Aktuelle Neurologie*, vol. 35, no. S 01, 2008.

[2] D. J. Lin, K. L. Hermann, and J. D. Schmahmann, "Multiple system atrophy of the cerebellar type: Clinical state of the art," *Movement Disorders*, vol. 29, no. 3, pp. 294–304, 2014.

[3] K. A. Jellinger, "Neuropathology of multiple system atrophy: New thoughts about pathogenesis," *Movement Disorders*, vol. 29, no. 14, pp. 1720–1741, 2014.

[4] G.-M. Kim, S. E. Kim, and W. Y. Lee, "Preclinical impairment of the striatal dopamine transporter system in sporadic olivopontocerebellar atrophy: Studied with [123I]β-CIT and SPECT," *European Neurology*, vol. 43, no. 1, pp. 23–29, 2000.

[5] M. Oh, J. S. Kim, J. Y. Kim et al., "Subregional patterns of preferential striatal dopamine transporter loss differ in Parkinson disease, progressive supranuclear palsy, and multiple-system atrophy," *Journal of Nuclear Medicine*, vol. 53, no. 3, pp. 399–406, 2012.

[6] S. Jin, M. Oh, S. J. Oh et al., "Differential Diagnosis of Parkinsonism Using Dual-Phase F-18 FP-CIT PET Imaging," *Nuclear Medicine and Molecular Imaging*, vol. 47, no. 1, pp. 44–51, 2013.

[7] Y. H. Weng, M. C. Chen, R. S. Chen, K. Y. Tzen, and S. P. Wey, "99mTc-TRODAT-1 imaging of multiple system atrophy," *Journal of Nuclear Medicine*, vol. 45, pp. 45–49, 2004.

[8] K. Van Laere, C. Casteels, L. De Ceuninck et al., "Dual-tracer dopamine transporter and perfusion SPECT in differential diagnosis of parkinsonism using template-based discriminant analysis," *Journal of Nuclear Medicine*, vol. 47, no. 3, pp. 384–392, 2006.

[9] G. El Fakhri, M.-O. Habert, P. Maksud et al., "Quantitative simultaneous 99mTc-ECD/123I-FP-CIT SPECT in Parkinson's disease and multiple system atrophy," *European Journal of Nuclear Medicine and Molecular Imaging*, vol. 33, no. 1, pp. 87–92, 2006.

[10] M. Tripathi, V. Dhawan, S. Peng et al., "Differential diagnosis of parkinsonian syndromes using F-18 fluorodeoxyglucose positron emission tomography," *Neuroradiology*, vol. 55, no. 4, pp. 483–492, 2013.

[11] S. M. Broski, C. H. Hunt, G. B. Johnson, R. F. Morreale, V. J. Lowe, and P. J. Peller, "Structural and functional imaging in parkinsonian syndromes," *RadioGraphics*, vol. 34, no. 5, pp. 1273–1292, 2014.

[12] K. Y. Kwon, J. S. Kim, K. C. Im, M. C. Lee, and S. J. Chung, "Comparison of cerebral glucose metabolism between possible and probable system atrophy," *Journal of Movement Disorders*, vol. 2, pp. 22–28, 2009.

[13] L. Ciolli, F. Krismer, F. Nicoletti, and G. K. Wenning, "An update on the cerebellar subtype of multiple system atrophy," *Cerebellum & Ataxias*, vol. 1, no. 1, 2014.

[14] J. Wang, C. Zuo, Y. Jiang, Y. Guan, Z. Chen, and J. Xiang, "18F-FP-CIT PET imaging and SPM analysis of dopamine transporters in Parkinsons disease in various Hoehn & Yahr stages," *Journal of Neurology*, vol. 254, pp. 185–190, 2007.

[15] S. A. Eshuis, R. P. Maguire, K. L. Leenders, S. Jonkman, and P. L. Jager, "Comparison of FP-CIT SPECT with F-DOPA PET in patients with de novo and advanced Parkinson's disease," *European Journal of Nuclear Medicine and Molecular Imaging*, vol. 33, no. 2, pp. 200–209, 2006.

[16] I. Litvan, "Update on epidemiological aspects of progressive supranuclear palsy," *Movement Disorders*, vol. 18, supplement 6, pp. S43–S50, 2003.

[17] H. T. S. Benamer, J. Patterson, D. J. Wyper, D. M. Hadley, G. J. A. Macphee, and D. G. Grosset, "Correlation of Parkinson's disease severity and duration with 123I-FP-CIT SPECT striatal uptake," *Movement Disorders*, vol. 15, no. 4, pp. 692–698, 2000.

[18] C. L. Tomlinson, R. Stowe, S. Patel, C. Rick, R. Gray, and C. E. Clarke, "Systematic review of levodopa dose equivalency reporting in Parkinson's disease," *Movement Disorders*, vol. 25, no. 15, pp. 2649–2653, 2010.

[19] Y. J. Jeong, H. J. Son, H. J. Yoon, and D.-Y. Kang, "Functional volumetric analysis of striatum using F-18 FP-CIT PET in patients with idiopathic Parkinson's disease and normal subjects," *Annals of Nuclear Medicine*, vol. 30, no. 8, pp. 572–578, 2016.

[20] M. Werner-Wasik, A. D. Nelson, W. Choi et al., "What is the best way to contour lung tumors on PET scans? Multiobserver validation of a gradient-based method using a NSCLC digital PET phantom," *International Journal of Radiation Oncology • Biology • Physics*, vol. 82, no. 3, pp. 1164–1171, 2012.

[21] E. Munoz, A. Iranzo, S. Rauek et al., "Subclinical nigrostriatal dopaminergic denervation in the cerebellar subtype of multiple system atrophy (MSA-C)," *Journal of Neurology*, vol. 258, no. 12, pp. 2248–2253, 2011.

[22] U. Wüllner, T. Schmitz-Hübsch, M. Abele, G. Antony, P. Bauer, and K. Eggert, "Features of probable multiple system atrophy patients identified among 4770 patients with parkinsonism enrolled in the multicentre registry of the German Competence Network on Parkinson's disease," *Journal of Neural Transmission*, vol. 114, no. 9, pp. 1161–1165, 2007.

[23] K. A. Jellinger, K. Seppi, and G. K. Wenning, "Grading of neuropathology in multiple system atrophy: Proposal for a novel scale," *Movement Disorders*, vol. 20, no. 12, pp. S29–S36, 2005.

[24] T. Ozawa, D. Paviour, N. P. Quinn et al., "The spectrum of pathological involvement of the striatonigral and olivopontocerebellar systems in multiple system atrophy: clinicopathological correlations," *Brain*, vol. 127, no. 12, pp. 2657–2671, 2004.

[25] A. J. Stoessl, S. Lehericy, and A. P. Strafella, "Imaging insights into basal ganglia function, Parkinson's disease, and dystonia," *The Lancet*, vol. 384, no. 9942, pp. 532–544, 2014.

[26] Y. J. Kim, M. Ichise, J. R. Ballinger et al., "Combination of dopamine transporter and D2 receptor SPECT in the diagnostic evaluation of PD, MSA, and PSP," *Movement Disorders*, vol. 17, no. 2, pp. 303–312, 2002.

[27] T. Nissen, N. Malek, K. A. Grosset et al., "Baseline [123I]FP-CIT SPECT (DaTSCAN) severity correlates with medication use at 3 years in Parkinson's disease," *Acta Neurologica Scandinavica*, vol. 129, no. 3, pp. 204–208, 2014.

[28] K. Kazumata, V. Dhawan, T. Chaly et al., "Dopamine transporter imaging with fluorine-18-FPCIT and PET," *Journal of Nuclear Medicine*, vol. 39, no. 9, pp. 1521–1530, 1998.

[29] J. Lavalaye, J. Booij, L. Reneman, J. B. A. Habraken, and E. A. Van Royen, "Effect of age and gender on dopamine transporter imaging with [123I]FP-CIT SPET in healthy volunteers," *European Journal of Nuclear Medicine and Molecular Imaging*, vol. 27, no. 7, pp. 867–869, 2000.

[30] Y. Osaki, Y. Ben-Shlomo, G. K. Wenning et al., "Do published criteria improve clinical diagnostic accuracy in multiple system atrophy?" *Neurology*, vol. 59, no. 10, pp. 1486–1491, 2002.

Hindawi
Contrast Media & Molecular Imaging
Volume 2017, Article ID 5438395, 10 pages
https://doi.org/10.1155/2017/5438395

Clinical Study

Comparison of Diagnostic Performance of Three-Dimensional Positron Emission Mammography versus Whole Body Positron Emission Tomography in Breast Cancer

Dong Dai,[1] Xiuyu Song,[1] Man Wang,[2] Lin Li,[3,4] Wenchao Ma,[1] Wengui Xu,[1] Yunchuan Ma,[2] Juntian Liu,[1] Jin Zhang,[1] Peifang Liu,[1] Xiaoyue Gu,[3,4] and Yusheng Su[2]

[1] *Department of Molecular Imaging and Nuclear Medicine and Key Laboratory of Cancer Prevention and Therapy and Key Laboratory of Breast Cancer Prevention and Therapy, Tianjin Medical University Cancer Institute and Hospital, National Clinical Research Center for Cancer, Tianjin 300060, China*
[2] *PET Center of Xuan Wu Hospital, Capital Medical University, Beijing, China*
[3] *Division of Nuclear Technology and Applications, Institute of High Energy Physics, Chinese Academy of Sciences, Beijing 100049, China*
[4] *Beijing Engineering Research Center of Radiographic Techniques and Equipment, Beijing 100049, China*

Correspondence should be addressed to Wengui Xu; wenguixy@yeah.net

Received 21 February 2017; Accepted 10 May 2017; Published 3 July 2017

Academic Editor: David Yang

Objective. To compare the diagnostic performance of three-dimensional (3D) positron emission mammography (PEM) versus whole body positron emission tomography (WBPET) for breast cancer. *Methods*. A total of 410 women with normal breast or benign or highly suspicious malignant tumors were randomized at 1 : 1 ratio to undergo 3D-PEM followed by WBPET or WBPET followed by 3D-PEM. Lumpectomy or mastectomy was performed on eligible participants after the scanning. *Results*. The sensitivity and specificity of 3D-PEM were 92.8% and 54.5%, respectively. WBPET showed a sensitivity of 95.7% and specificity of 56.8%. After exclusion of the patients with lesions beyond the detecting range of the 3D-PEM instrument, 3D-PEM showed higher sensitivity than WBPET (97.0% versus 95.5%, $P = 0.913$), particularly for small lesions (<1 cm) (72.0% versus 60.0%, $P = 0.685$). *Conclusions*. The 3D-PEM appears more sensitive to small lesions than WBPET but may fail to detect lesions that are beyond the detecting range. This study was approved by the Ethics Committee (E2012052) at the Tianjin Medical University Cancer Institute and Hospital (Tianjin, China). The instrument positron emission mammography (PEMi) was approved by China State Food and Drug Administration under the registration number 20153331166.

1. Introduction

Breast cancer is the most common type of cancer in women worldwide, and there were approximately 1.7 million new cases in 2012 [1]. In China, the incidence of breast cancer increases continuously for the past two decades, and the estimated incidence and mortality in 2013 was 25.89 and 6.56 cases per 100,000 women, respectively [2, 3]. Early diagnosis is the key to improve the prognosis and outcomes of patients with breast cancer. The Swedish randomized trials demonstrated that mammography screening reduced the mortality of breast cancer significantly [4]. In addition to mammography, mammary ultrasonography, and breast magnetic resonance imaging (MRI), whole body position emission tomography (WBPET) has been used for diagnosis and staging of breast cancer [5–8]. WBPET detects suspicious mammary lesions based on the unique biochemical characteristics of breast cancer. Malignant mammary lesions usually have a higher rate of glucose metabolism than normal or benign tumors, leading to a significantly greater accumulation of radiotracer labeled glucose analogues, such as ^{18}F-fluorodeoxyglucose (^{18}F-FDG), in malignant lesions, which can be detected by WBPET scanning [5–8].

FDG-WBPET scan appears to be particularly superior to the nonbiochemical techniques such as mammography and mammary ultrasonography in patients without obvious cancer-associated anatomical changes. FDG-WBPET scan can detect malignancies in patients with dense or scarring breast tissues, whereas those nonbiochemical techniques usually fail on those patients [9]. In a meta-analysis to systematically compare the diagnostic accuracy of ultrasonography, computed tomography, breast MRI, mammography, and FDG-WBPET in patients with suspected recurrent and/or metastatic breast cancer, Pan et al. found that breast FDG-WBPET showed the highest pooled sensitivity [10]. However, the relatively low spatial resolution of FDG-WBPET (4 mm to 7 mm) limits its use on staging breast cancer and particularly limits its value to detect small lesions or lymph node metastases in breast cancer [11, 12].

To improve the spatial resolution, positron emission mammography (PEM) has been developed recently by multiple research institutes and medical instrument industry [9, 13–23]. Aliaga et al. tested PEM on animal models of breast cancer and found that the potential spatial resolution of PEM was 1.8 mm [24]. In a recent meta-analysis, Caldarella et al. showed that the pooled sensitivity and specificity for PEM were 85% and 79%, respectively in women with suspicious breast lesions [25]. Recently, Yamamoto et al. compared the imaging sensitivity of PEM versus WBPET in relation to tumor size and found that PEM showed significantly higher imaging sensitivity (78.6%) than WBPET (47.6%), particularly for small size tumors [26]. Large-scale trial to compare diagnostic performance of PEM versus WBPET in Chinese women is still lacking. This study aims to fill this knowledge gap. Here, in this double-center study, participants with normal breast or benign or malignant tumors received three-dimensional PEM (3D-PEM) and WBPET scanning sequentially. Diagnostic performance of 3D-PEM and WBPET was evaluated by comparing the imaging diagnosis with histopathological diagnosis. The detector of the 3D-PEM instrument used in this study has an average intrinsic spatial resolution of 1.67 mm [27].

2. Methods

2.1. Study Design and Settings. This prospective, noninterventional, double-center, randomized clinical study was conducted in Tianjin Medical University Cancer Hospital and Xuanwu Hospital of Capital Medical University from August 2012 to March 2014. The study protocol was approved by the Institutional Review Boards of Tianjin Medical University and Capital Medical University. The study was conducted in compliance with the Declaration of Helsinki, the Good Clinical Practices, and relevant ethical guidelines.

2.2. Participants. Informed consent was obtained from all study participants. Eligible participants were aged 18 to 70 years with or without a family history of breast diseases and had normal mammary gland, benign, or highly suspicious malignant mammary tumor. The mammary condition was evaluated by clinical tests, mammography, and mammary ultrasonography. The exclusion criteria were pregnancy and breast feeding, previous surgery, chemotherapy, or radiotherapy to treat malignancy, low tolerance to WBPET or PEM, being unable to keep prone position, being unable to undergo surgery although having an indication of surgery, or being unsuitable for the study based on the judgment of participating investigators. At the enrollment interview, general clinical data were collected. Mammography and mammary ultrasonography were performed or the results of these tests were obtained from the participants if they took the tests within 3 months prior to the enrollment interview. Eligible participants were scheduled for PEM and WBPET within 30 days of the interview. After PEM and WBPET, lumpectomy or mastectomy was performed on the patients that were eligible for surgery based on physician's judgment. Mammary biopsy was conducted prior to the surgery. Surgical tissue specimens collected after lumpectomy or mastectomy were examined by pathologists.

2.3. 3D-PEM Scanning. 3D-PEM was performed using a PEMi-I scanning system (Gao Neng Medical Equipment Co., Ltd. Hangzhou, China). The PEMi-I system has a 64-ring detecting system, which allows for efficient acquisition of 3D images. The opening for breast placement has a diameter of 160 mm. The machine was designed for prone position, so that the breasts hang freely in the detector (Figure 1). Participants were required to fast for 4 to 6 hours and their fast blood glucose was determined. The radiotracer ^{18}F-FDG (259–444 MBq) was injected intravenously to the participants that had a fast blood glucose level $\leq$ 140 mg/dL, and then the participants were required to rest for 50–60 minutes to allow the radiotracer to circulate. The participants that were allocated for the group of 3D-PEM followed by WBPET had 20-minute scan on the PEMi-I for each breast. Twelve-slice reconstructions were created, with slice thickness varying from 3 to 8 mm depending on breast thickness. Images were submitted to attenuation correction according to the image segmentation method. On the PEM images, breast tissue was separated from air based on the activity map of the breast. Linear attenuation coefficients (ACF) were obtained for each line of response based on the segmentation result. Reconstruction was repeated with the ACFs. WBPET was performed immediately after 3D-PEM (approximately 90 to 100 minutes after radiotracer injection).

2.4. Whole Body WBPET Scanning. Patients that were allocated to the group of WBPET followed by 3D-PEM underwent WBPET after radiotracer injection. WBPET was performed using the WBPET scanning system Discovery ST 4 UPG (GE, USA) or EXACT ECAT 47 (Siemens, Germany). The image acquisition (120 kV, 160–220 mA, helical pitch 0.75 : 1, and 5 mm slice thickness) was conducted using 2-minute emission acquisitions from the apex of the lung to the lower edge of the liver with participants at supine position. 3D-PEM was then performed immediately after WBPET (approximately 80–90 minutes after radiotracer injection).

2.5. Image Analysis. WBPET and PEM images were reviewed by 3 certified radiologists, who were blinded to participants'

(a) (b)

Figure 1: Images of the PEM system.

clinical information. A positive PEM and WBPET were defined as images showing continuous 2 layers of visible nodular or blocks of moderately to strongly abnormal radioactivity uptake. A negative PEM and WBPET were images showing no or very weak abnormal radioactivity uptake. Disagreements among the radiologists were discussed until reaching a consensus.

2.6. Surgical Histopathological Examination. Patients underwent lumpectomy or mastectomy within 1-2 weeks after WBPET and 3D-PEM examination. Surgical tissue specimens collected after lumpectomy or mastectomy were examined by pathologists. The histological grade and type were determined.

2.7. Evaluation. Concordant positive diagnosis was defined as the scanning images of both 3D-PEM and WBPET showing lesions with similar shape and size; concordant negative diagnosis represented absence of lesions on the scanning images of both 3D-PEM and WBPET. Positive WBPET was defined as images presenting more than 2 layers of visible nodular shaped or massive area of medium to severe abnormal increased uptake of radiotracer. Negative WBPET represented images showing uniformly distributed radioactivity or scattered, spotty, and mild increased uptake of radiotracer. The sensitivity and specificity of 3D-PEM and WBPET were compared. Calculations for concordance rate of positive diagnosis, concordance rate of negative diagnosis, overall diagnostic concordance, sensitivity, specificity, and accuracy are explained in Table 1.

2.8. Sample Size. At a significant level of 5% (2-sided), 239 participants with breast cancer were required to achieve 95% concordant positive diagnosis of 3D-PEM compared to WBPET with a power of 80%. Based on the assumption of 80% concordant negative diagnosis of 3D-PEM compared to WBPET at a significant level of 5% and a power of 80%, 153 participants with benign tumor or normal breasts were required. To achieve 90% overall diagnostic concordance of 3D-PEM compared to WBPET at a significant level of 5% and a power of 80%, 385 participants were required. Thus, the estimated total sample size was 392 (239 positive + 153 negative) participants, and a total of 400 participants (160 cases of negative malignancy + 240 cases of positive malignancy) were to be enrolled.

Table 1: Calculation of diagnostic concordance and performance of WBPET and 3D-PEM.

	WBPET+	WBPET−
3D-PEM+	A	B
3D-PEM−	C	D
	Histopathology +	Histopathology −
3D-PEM or WBPET+	a	b
3D-PEM or WBPET−	c	d

Concordance rate of positive diagnosis of 3D-PEM compared with WBPET $= A/(A + C) \times 100\%$; concordance rate of negative diagnosis of 3D-PEM compared with WBPET $= D/(B + D) \times 100\%$; overall diagnostic concordance $= (A + D)/(A + B + C + D) \times 100\%$; sensitivity $= a/(a + c) \times 100\%$; specificity $= d/(b + d) \times 100\%$; accuracy $= (a + d)/(a + b + c + d) \times 100\%$.

2.9. Randomization and Blinding. To minimize possible bias effects of the amount of ^{18}F-FDG uptake on the diagnosis, participants were randomized at 1 : 1 ratio to undergo either 3D-PEM followed by WBPET (3D-PEM-WBPET) or WBPET followed by 3D-PEM (WBPET-3D-PEM). Randomization sequence was generated with the software SAS. Participants were not blinded for WBPET and 3D-PEM. The radiologists, who evaluated the scanning images of WBPET and 3D-PEM, were blinded for participants' clinical data.

2.10. Statistical Analysis. The statistical analysis was performed using the software SAS 9.13. Full analysis set (FAS) included data from participants with WBPET results. Per protocol set (PPS) included data from participants that were compliant with the study protocol, and participants with severe deviation from protocol, such as failure to undergo 3D-PEM, were excluded from PPS. Categorical variables are presented as percentage and continuous variables are presented as mean ± standard deviation (SD), median, minimum, and maximum. Diagnostic concordance, sensitivity, specificity, and accuracy were calculated. Student's t-test was used to compare patients' clinical characteristics. Chi-square test was used to compare sensitivity, specificity, and accuracy.

Table 2: Baseline clinical characteristics.

	3D-PEM-WBPET (n = 204)	WBPET-3D-PEM (n = 200)	P value	Total (N = 404)
Age (years)				
Mean ± SD	50.1 ± 9.3	51.1 ± 9.1	0.2663	50.6 ± 9.2
Median (min, max)	50.0 (19.0, 71.0)	51.0 (20.0, 70.0)		50.0 (19.0, 71.0)
BMI (kg/m^2)				
Mean ± SD	24.3 ± 3.4	24.5 ± 3.7	0.6061	24.4 ± 3.6
Median (min, max)	24.1 (17.3, 39.7)	24.2 (15.9, 43.0)		24.2 (15.9, 43.0)
SBP (mmHg)				
Mean ± SD	120.3 ± 12.1	122.5 ± 15.3	0.1075	121.4 ± 13.8
Median (min, max)	120.0 (87.0, 160.0)	120.0 (87.0, 180.0)		120.0 (87.0, 180.0)
DBP (mmHg)				
Mean ± SD	77.4 ± 7.9	78.1 ± 8.6	0.3913	77.7 ± 8.2
Median (min, max)	80.0 (51.0, 109.0)	80.0 (53.0, 100.0)		80.0 (51.0, 109.0)
Comorbidities, n				
Diabetes mellitus	9.7% (11/113)	11.7 (13/111)	0.6323	
Uterine fibroids	48.9% (23/47)	55.9% (19/34)	0.5366	

SBP: systolic blood pressure; DBP: diastolic blood pressure; SD: standard deviation; BMI: body mass index. Values in the 2 groups were compared by Student's t-test or chi-square or Fisher's exact test.

3. Results

3.1. Patient Flow and Baseline Data. A total of 410 participants, including 255 patients with highly suspicious malignancy based on mammography and mammary ultrasonography and 155 participants without malignancy were enrolled in the study and randomized to WBPET-3D-PEM or 3D-PEM-WBPET group. During the study, 6 subjects did not receive WBPET because of voluntary withdrawal from the study. Thus, FAS contained 404 participants. Among participants undergoing WBPET, 3D-PEM results were missing from 5 participants, resulting in PPS of 399 participants. Patient flow is displayed in Figure 2. Participants' baseline clinical data are described in Table 2. Clinical characteristics were comparable in participant receiving 3D-PEM-WBPET versus that receiving WBPET-3D-PEM (Table 2).

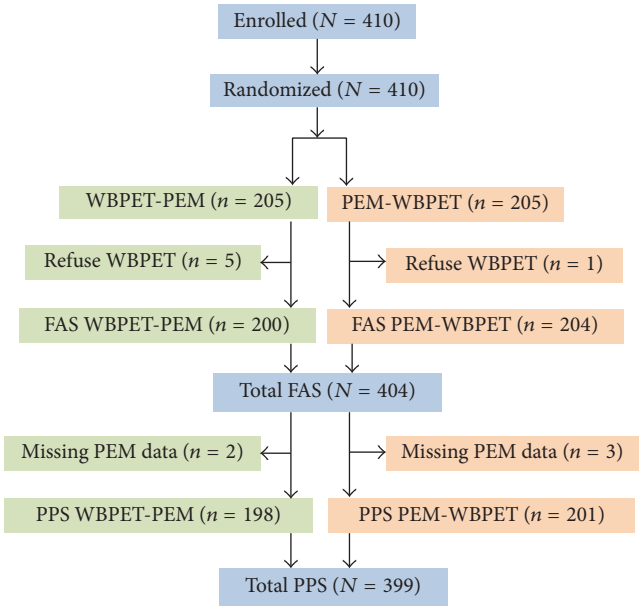

Figure 2: Patient flow chart.

3.2. Evaluation. Diagnostic concordance of 3D-PEM and WBPET was analyzed on FAS and PPS data. For FAS data, concordance rate of positive diagnosis was 93.8% (95% CI: 90.6%–97.1%), concordance rate of negative diagnosis was 97.5% (95% CI: 94.8%–100.0%), and overall diagnostic concordance was 95.3% (95% CI: 93.1%–97.5%, Table 3). These results are similar to those from the analysis on PPS data (Table 3).

A total of 19 participants showed inconsistent 3D-PEM and WBPET (Tables 3 and 4), among whom, 5 lost 3D-PEM data (Table 4). Histopathological examination of the remaining 14 cases revealed 3 cases of consistency between 3D-PEM and histopathological results and 11 cases of consistency between WBPET and histopathological results. Of the 11 cases of false diagnosis by 3D-PEM, 9 showed false negative 3D-PEM but true positive WBPET, and the lesions of the 9 cases were either near the chest wall (7 cases) or near the armpit (2 cases). These locations are out of the detecting range of the 3D-PEM detector (Table 4). The histopathological results of the 2 false positive 3D-PEM were one case of inflammatory lesion and one case of adenofibroma. Of the 3 cases wrongly diagnosed by WBPET, 2 were false positive and one was false negative. These 3 cases were accurately diagnosed by 3D-PEM. The 3D-PEM and WBPET scanning images of the case showing false negative WBPET and true positive 3D-PEM are presented in Figure 3. The images of the case with false positive WBPET and true negative PEM are presented in Figure 4.

Table 3: Diagnostic concordance of 3D-PEM and WBPET.

	Full analysis set		Total
	WBPET +	WBPET −	
3D-PEM +	228	4	
3D-PEM −	15	157	
	243	161	404
Concordance rate of positive diagnosis: 228/243 = 93.8% (95% CI: 90.6%–97.1%)			
Concordance rate of negative diagnosis: 157/161 = 97.5% (95% CI: 94.8%–100.0%)			
Overall diagnostic concordance: 385/404 = 95.3% (95% CI: 93.1%–97.5%)			
	Perprotocol set		Total
	WBPET +	WBPET −	
3D-PEM +	228	3	
3D-PEM −	11	157	
	239	160	399
Concordance rate of positive diagnosis: 228/239 = 95.4% (95% CI: 92.5%–98.3%)			
Concordance rate of negative diagnosis: 157/160 = 98.1% (95% CI: 95.7%–100.0%)			
Overall diagnostic concordance: 385/399 = 96.5% (95% CI: 94.6%–98.4%)			

CI: confidential interval.

Table 4: Participants with inconsistent diagnosis from 3D-PEM and WBPET.

Subject ID	Age (years)	WBPET (left/right)	3D-PEM (left/right)	Histopathology (left/right)
3D-PEM loss				
004	46	+/−	NA/NA (loss)	+/NA
008	47	−/−	NA/NA (loss)	+/NA
010	58	−/+	NA/NA (loss)	NA/−
250	64	−/+	NA/NA (loss)	NA/+
251	47	+/−	NA/NA (loss)	+/NA
Consistent 3D-PEM and histopathology (false diagnosis of WBPET)				
003	35	−/+	−/−	NA/−
161	65	−/−	−/+	NA/+
128	45	−/+	−/−	−/−
Consistent WBPET and histopathology (false diagnosis of 3D-PEM)				
False negative 3D-PEM				
036	45	+/−	−/−	+/NA
063	38	−/+	−/−	NA/+
086	45	−/+	−/−	NA/+
089	46	−/+	−/−	NA/+
096	44	−/+	−/−	NA/+
244	48	+/−	−/−	+/NA
414	52	−/+	−/−	NA/+
177	55	+/−	−/−	+/NA
181	47	−/+	−/−	NA/+
False positive 3D-PEM				
018	44	−/−	+/−	−/NA
112	54	−/−	+/−	−/NA

+/+: left breast + and right breast +; +/−: left breast + and right breast −; −/+: left breast − and right breast +; −/−: left breast − and right breast −. NA: not applied (no histopathology examination). A positive test represents at least one side breast showing +. A negative test represents both sides showing −. Participants without 3D-PEM were considered to show inconsistent results compared with WBPET.

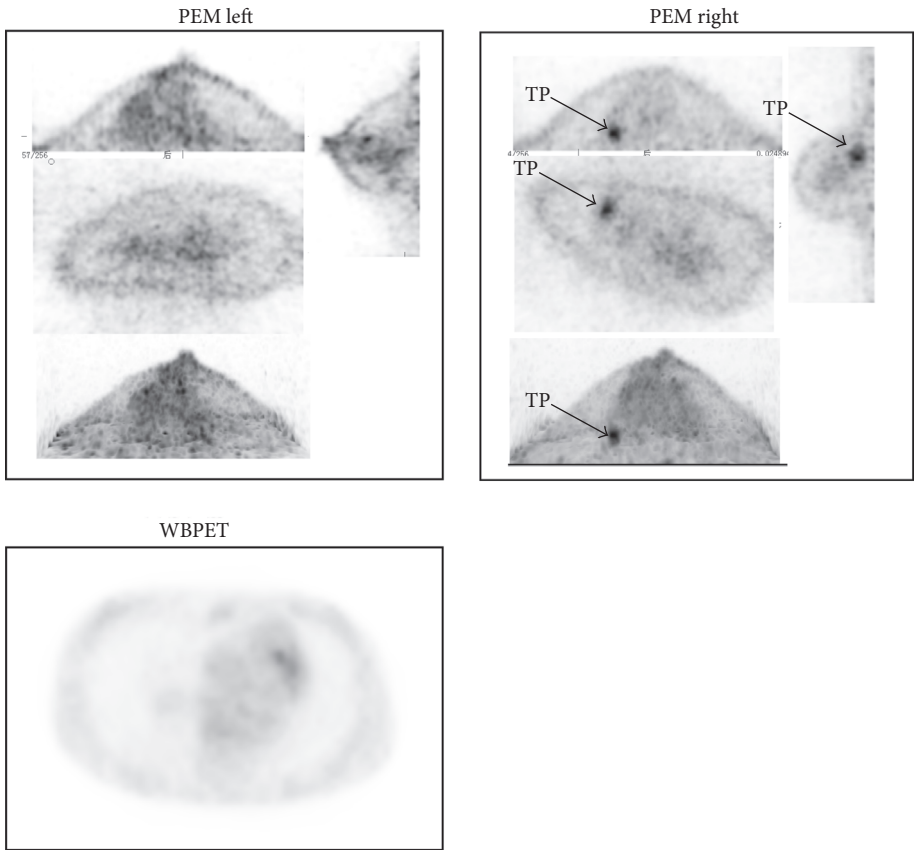

Figure 3: The images of the case showing false negative WBPET and true positive PEM. PEM images (left and right) and WBPET images of a 60-year-old woman with a true positive (TP) lesion (abnormal high ^{18}F-FDG uptake, the maximum standard uptake value (SUVmax) is 4.12) in the right mammary gland (arrow pointing), whereas abnormal high ^{18}F-FDG uptake was not shown in the PET (false negative, FN).

The diagnostic accuracy of WBPET and 3D-PEM was evaluated using histopathology results as the gold diagnostic standard. Histopathology was available from 253 participants, including 209 malignant and 44 benign cases. The majority of the malignancy was infiltrating ductal carcinoma (159/209, 76.1%). There were only 18 cases (18/209, 8.5%) of ductal carcinoma in situ (DCIS), and the remaining cases (191/209, 91.5%) were invasive carcinomas. 3D-PEM and WBPET appeared to have similar specificity (54.5% versus 56.8%, $P = 0.909$) and accuracy (86.2% versus 88.9%, $P = 0.808$, Table 5). Although WBPET sensitivity (95.7%) was slightly higher than 3D-PEM sensitivity (92.8%), the values are not significantly different ($P = 0.828$, Table 5). To further estimate the performance of WBPET and 3D-PEM, we analyzed lesions < 1 cm and lesions ≥ 1 cm separately. Diameters of three dimensions were measured and the average diameter was calculated to represent lesion size. The mean lesion size (total 278 lesions) was 1.7 ± 8.4 cm. For the 44 small lesions (diameter < 1 cm), 3D-PEM showed higher sensitivity (69.2%) than WBPET (61.5%, $P = 0.79$, Table 5); for the 234 larger lesions (diameter ≥ 1 cm), WBPET sensitivity (92.1%) was slightly higher than PEM sensitivity (90.1%, $P = 0.88$, Table 5). However, sensitivity was not statistically significantly different between WBPET and 3D-PEM. No WBPET or PEM associated adverse event was reported during the study.

To accurately evaluate the diagnostic performance of 3D-PEM, we excluded the one patient with benign lesion out of PEM detecting range and the 9 patients, whose malignant lesions were beyond the range of PEM detector. We then compared the performance of WBPET and 3D-PEM on the 243 cases (253 − 10). The overall sensitivity of 3D-PEM (97.0%) was slightly higher than that (95.5%) of WBPET ($P = 0.913$, Table 6). In both small lesion (<1 cm) and large lesion (≥1 cm) subgroups, 3D-PEM sensitivity was higher than WBPET sensitivity (small lesions: 72.0% versus 60.0%, $P = 0.685$; large lesions: 93.8% versus 91.8%, $P = 0.835$, Table 6).

4. Discussion

In the current study, the diagnostic concordance of 3D-PEM and WBPET was higher than 95%. Since the first report on PEM by Thompson et al. in 1994 [14], several pilot clinical studies including small number of patients showed promising results of using PEM to diagnose breast cancer [21–23]. Levine et al. evaluated PEM on 18 biopsy-proven malignant lesions and found that PEM yielded a sensitivity, specificity, and overall diagnostic accuracy of 86%, 91%, and 89%, respectively [21]. Similarly, Rosen et al. tested PEM on 18 malignant and 2 benign mammary abnormalities and found a sensitivity of 86% [22], and Tafra et al. demonstrated that

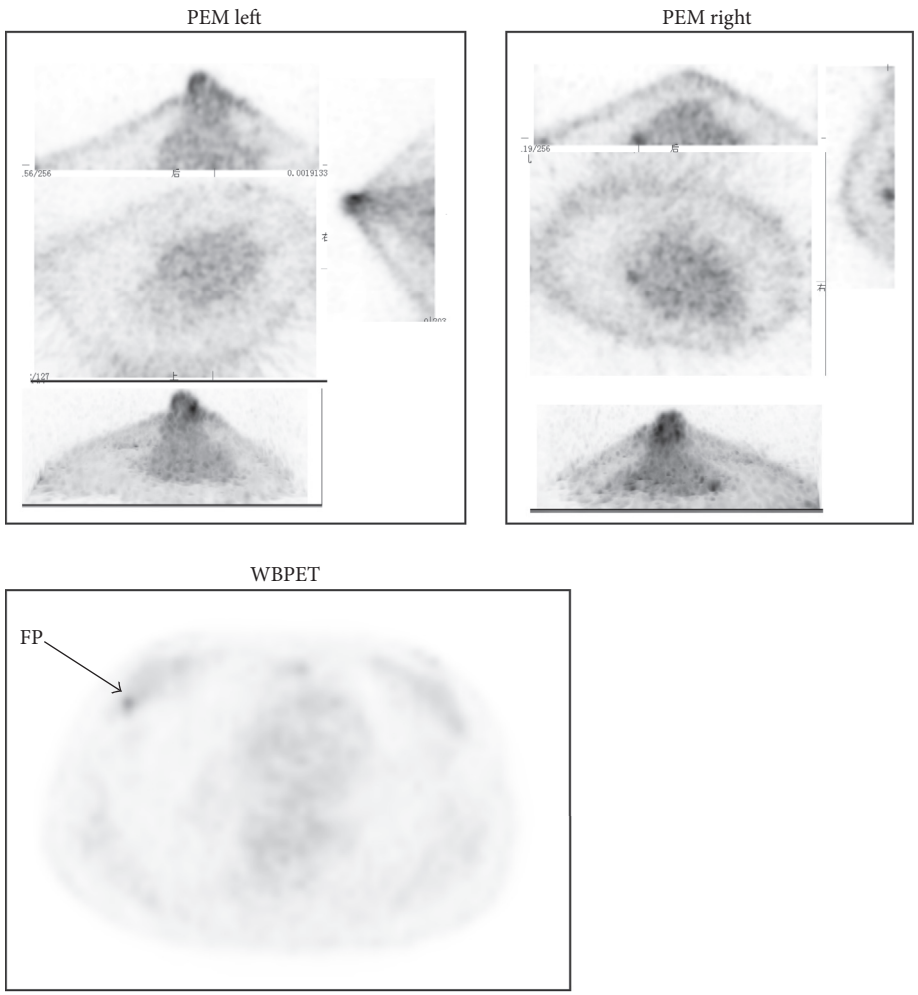

Figure 4: The images of the case showing false positive WBPET and true negative PEM. PEM images (left and right) and WBPET images of a 48-year-old woman without lesion (no abnormal high ^{18}F-FDG uptake, true negative (TN)) in the left or the right mammary gland (arrow pointing), whereas abnormal high ^{18}F-FDG uptake was shown in the PET (arrow pointing; the maximum standard uptake value (SUVmax) is 2.64; false positive (FP)).

PEM led to a sensitivity of 87% in 44 newly diagnosed breast cancer patients [23]. In a recent meta-analysis to investigate the diagnostic accuracy of PEM to detect malignancy in women with suspicious breast cancer, Caldarella et al. found that the pooled sensitivity and specificity were 85% (95% CI: 83%–88%) and 79% (95% CI: 74%–83%), respectively [25]. However, only 8 studies were included in the meta-analysis and significant study heterogeneity was associated with the pooled sensitivity and specificity [25]. Compared with those previous reports, this current study showed a higher sensitivity of PEM, which was 92.8% in the 253 patients with histopathologically confirmed diagnosis and 97.0% in the 243 patients with lesions within the 3D-PEM detecting range. The higher sensitivity of PEM observed in this current study may be partially attributable to the high proportion of invasive breast cancers (>90%) in the patients. Caldarella et al. reported that the pooled sensitivity of PEM was higher (86%) for invasive cancers than for in situ cancers (81%) [25].

Because of the higher spatial resolution of PEM than WBPET, PEM is predicted to be more sensitive to detecting malignancies than WBPET, particularly for small size lesions [14]. Data from previous studies appear to support this prediction [26, 28]. In a recent report, Yamamoto et al. investigated the association between tumor size and the sensitivity of PEM and WBPET in 45 Japanese women with histopathologically confirmed mammary malignancy [26]. They found that PEM was significantly more sensitive than WBPET (66.7% versus 13.3%, $P = 0.008$) for lesions < 1 cm, whereas detection sensitivity for lesions ≥ 1 cm was comparable in the 2 imaging approaches [26]. They also showed that the sensitivity advantage of PEM over WBPET diminished as the lesion size increased [26]. Similarly, Schilling et al. reported that PEM had a significantly higher lesion detection sensitivity than WBPET (92.8% versus 67.9%, $P < 0.001$) [28]. Report by Kalinyak et al. also shows a significantly higher sensitivity of PEM to detect tumor in 69 patients with newly diagnosed breast cancer than WBPET (92% versus 56%) [29].

Table 5: Comparison of diagnostic performance of 3D-PEM and WBPET.

Total cases					
	WBPET $n = 253$		3D-PEM $n = 253$		P value
	+	−	+	−	
Histopathology +, $n = 209$	200	9	194	15	
Histopathology −, $n = 44$	19	25	20	24	
Sensitivity (%)	95.7		92.8		0.828
Specificity (%)	56.8		54.5		0.909
Accuracy (%)	88.9		86.2		0.808
	WBPET $n = 44$		3D-PEM $n = 44$		P value
	+	−	+	−	
Lesion < 1 cm					
Histopathology +, $n = 26$	16	10	18	8	
Histopathology −, $n = 18$	5	13	6	12	
Sensitivity (%)	61.5		69.2		0.79
Specificity (%)	72.2		66.7		0.878
Accuracy (%)	65.9		68.1		0.92
	WBPET $n = 234$		3D-PEM $n = 234$		P value
	+	−	+	−	
Lesion ≥ 1 cm					
Histopathology +, $n = 203$	187	16	183	20	
Histopathology −, $n = 31$	15	16	15	16	
Sensitivity (%)	92.1		90.1		0.88
Specificity (%)	51.6		51.6		1.0
Accuracy (%)	86.8		85.0		0.65

Values were compared by chi-square test.

Table 6: Comparison of diagnostic performance of 3D-PEM and WBPET after exclusion of lesions beyond the range of 3D-PEM detector.

Total cases					
	WBPET $n = 243$		3D-PEM $n = 243$		P value
	+	−	+	−	
Histopathology +, $n = 200$	191	9	194	6	
Histopathology −, $n = 43$	18	25	20	23	
Sensitivity (%)	95.5		97.0		0.913
Specificity (%)	58.1		53.5		0.517
Accuracy (%)	88.9		89.3		1.0
	WBPET $n = 43$		3D-PEM $n = 43$		P value
	+	−	+	−	
Lesion < 1 cm					
Histopathology +, $n = 25$	15	10	18	7	
Histopathology −, $n = 18$	5	13	6	12	
Sensitivity (%)	60.0		72.0		0.685
Specificity (%)	72.2		66.7		0.878
Accuracy (%)	65.1		69.8		0.613
	WBPET $n = 225$		3D-PEM $n = 225$		P value
	+	−	+	−	
Lesion ≥ 1 cm					
Histopathology +, $n = 195$	179	16	183	12	
Histopathology −, $n = 30$	14	16	15	15	
Sensitivity (%)	91.8		93.8		0.835
Specificity (%)	53.3		50.0		0.884
Accuracy (%)	86.7		88.0		0.912

The current study also demonstrated that the PEM showed higher sensitivity than WBPET in small lesions, although the difference was not statistically significant because of the relatively low number of small lesions. Compared with the previously reported sensitivity of WBPET in breast cancer, which was between 64% and 96% [30], the detection sensitivity of WBPET in this current study (96.5%) is on the high end of the range. The relatively large average size of lesions in our patients (diameter > 1.5 cm) may contribute to the high sensitivity of WBPET. In addition, the WBPET systems used in this current study are dual time point imaging WBPET, which has been shown to have an improved sensitivity to detect invasive mammary malignancies [31].

This current study found 9 cases of false negative 3D-PEM, which were true positive from WBPET and histopathological analysis. Schilling et al. suggested that the false negative PEM in their study could be related to insufficient FDG uptake of the small size lesions [28]. Insufficient FDG uptake appeared to be not the reason for false negative PEM in this current study because the 9 cases were correctly diagnosed by WBPET. Careful review of the WBPET images revealed that the lesions of the 9 cases are beyond the detecting range of the 3D-PEM instrument. Of the 9 cases of false negative 3D-PEM, 7 lesions are next to the pectoral muscle and 2 lesions are near the armpit. In addition to very small size lesions with inadequate radiotracer uptake, the limitation of field-of-view associated with PEM instrument is also considered a major source of false negative results [25]. Deep small lesions located near to the pectoral muscle or in the axillary region are particularly difficult to be detected by PEM. The 9 false negative 3D-PEM cases may also contribute to the slightly lower overall sensitivity of 3D-PEM (92.8%) compared with WBPET (95.7%) in this current study. After exclusion of the 9 false negative 3D-PEM cases and the one case of benign lesion that was out of the detecting range of the 3D-PEM, the 3D-PEM showed a higher sensitivity than WBPET for all the lesions (97.0% versus 95.5%), small lesions (72.0% versus 60.0%), and large lesions (93.8% versus 91.8%). Histopathological analysis of the 2 false positive PEM cases revealed that they are one case of inflammatory lesion and one case of adenofibroma, suggesting that benign mammary abnormalities might also have a higher metabolic rate of glucose than normal breast tissue.

5. Conclusion

This current study found that 3D-PEM and WBPET showed satisfactory diagnostic concordance in Chinese patients and that the 3D-PEM appeared to be more sensitive than WBPET for lesions within the detecting range of the 3D-PEM instrument, particularly for small lesions with a diameter < 1 cm. The 3D-PEM instrument used in the current study may not detect lesions beyond the detecting range, particularly the regions near to the pectoral muscle and the axillary regions.

Ethical Approval

All procedures performed in studies involving human participants were in accordance with the ethical standards of the institutional and/or national research committee and with the 1964 Helsinki declaration and its later amendments or comparable ethical standards.

Consent

Informed consent was obtained from all individual participants included in the study.

Conflicts of Interest

All authors declare that they have no conflicts of interest.

Acknowledgments

This work was supported by grants from the National Natural Science Foundation of China (Grants nos. 81302003, 81501984, and 81601377), the National Science and Technology Major Project (Grant no. 2013ZX09303001), Tianjin Natural Science Fund (16JCZDJC35200, 17JCYBJC25100), Incubation Project of National Clinical Research Center for Cancer (N14B09), Tianjin Medical University Cancer Institute and Hospital Fund (Y1601), and the Science & Technology Development Fund of Tianjin Education Commission for Higher Education (no. 20120109).

References

[1] J. Ferlay, I. Soerjomataram, R. Dikshit et al., "Cancer incidence and mortality worldwide: sources, methods and major patterns in GLOBOCAN 2012," *International Journal of Cancer*, 2014.

[2] L. Fan, Y. Zheng, K.-D. Yu et al., "Breast cancer in a transitional society over 18 years: Trends and present status in Shanghai, China," *Breast Cancer Research and Treatment*, vol. 117, no. 2, pp. 409–416, 2009.

[3] *National Cancer Center and Disease Prevention and Control Bureau MoH: Chinese Cancer Registry Annual Report, 2013*, Military Medical Sciences Press, Beijing, China, 2014.

[4] L. Nyström, I. Andersson, N. Bjurstam, J. Frisell, B. Nordenskjöld, and L. E. Rutqvist, "Long-term effects of mammography screening: Updated overview of the Swedish randomised trials," *Lancet*, vol. 359, no. 9310, pp. 909–919, 2002.

[5] H. Shimada, T. Setoguchi, M. Yokouchi et al., "Metastatic bone tumors: analysis of factors affecting prognosis and efficacy of CT and 18F-FDG WBPET-CT in identifying primary lesions," *Molecular and Clinical Oncology*, vol. 2, pp. 875–881, 2014.

[6] A. M. García Vicente, M. Á. Cruz Mora, A. A. León Martín et al., "Glycolytic activity with ^{18}F-FDG PET/CT predicts final neoadjuvant chemotherapy response in breast cancer," *Tumor Biology*, vol. 35, no. 11, pp. 11613–11620, 2014.

[7] K. Ogino, M. Nakajima, M. Kakuta et al., "Utility of FDG-PET/CT in the evaluation of the response of locally advanced breast cancer to neoadjuvant chemotherapy," *International Surgery*, vol. 99, no. 4, pp. 309–318, 2014.

[8] J. M. Marti-Climent, I. Dominguez-Prado, M. J. Garcia-Velloso et al., "[18F]fluorothymidine-positron emission tomography in patients with locally advanced breast cancer under bevacizumab treatment: usefulness of different quantitative methods of tumor proliferation," *Revista Española de Medicina Nuclear e Imagen Molecular*, vol. 33, pp. 280–285, 2014.

[9] R. R. Raylman, J. Abraham, H. Hazard et al., "Initial clinical test of a breast-PET scanner," *Journal of Medical Imaging and Radiation Oncology*, vol. 55, no. 1, pp. 58–64, 2011.

[10] L. Pan, Y. Han, X. Sun, J. Liu, and H. Gang, "FDG-PET and other imaging modalities for the evaluation of breast cancer recurrence and metastases: a meta-analysis," *Journal of Cancer Research and Clinical Oncology*, vol. 136, no. 7, pp. 1007–1022, 2010.

[11] C. R. Isasi, R. M. Moadel, and M. D. Blaufox, "A meta-analysis of FDG-PET for the evaluation of breast cancer recurrence and metastases," *Breast Cancer Research and Treatment*, vol. 90, no. 2, pp. 105–112, 2005.

[12] I. C. Smith and F. J. Gilbert, "Role of positron emission tomography in the management of breast cancer," *Breast*, vol. 8, no. 6, pp. 303–310, 1999.

[13] A. Argus and M. C. Mahoney, "Positron emission mammography: diagnostic imaging and biopsy on the same day," *American Journal of Roentgenology*, vol. 202, no. 1, pp. 216–222, 2014.

[14] C. J. Thompson, K. Murthy, I. N. Weinbera, and F. Mako, "Feasibility Study for Positron Emission Mammography," *Medical Physics*, vol. 21, no. 4, pp. 529–538, 1994.

[15] A. M. Bergman, C. J. Thompson, K. Murthy et al., "Technique to obtain positron emission mammography images in registration with x-ray mammograms," *Medical Physics*, vol. 25, no. 11, pp. 2119–2129, 1998.

[16] N. K. Doshi, Y. Shao, R. W. Silverman, and S. R. Cherry, "Design and evaluation of an LSO PET detector for breast cancer imaging," *Medical Physics*, vol. 27, no. 7, pp. 1535–1543, 2000.

[17] C. J. Thompson, K. Murthy, M. Aznar et al., "Preliminary clinical evaluation of an instrument for "positron emission mammography" in the detection of breast cancer," *Clinical Positron Imaging*, vol. 1, article 265, 1998.

[18] I. Weinberg, S. Majewski, A. Weisenberger et al., "Preliminary results for positron emission mammography: Real-time functional breast imaging in a conventional mammography gantry," *European Journal of Nuclear Medicine*, vol. 23, no. 7, pp. 804–806, 1996.

[19] J. Qi and R. H. Huesman, "Scatter correction for positron emission mammography," *Physics in Medicine and Biology*, vol. 47, no. 15, pp. 2759–2771, 2002.

[20] I. N. Weinberg, D. Beylin, V. Zavarzin et al., "Positron emission mammography: high-resolution biochemical breast imaging," *Technology in Cancer Research & Treatment*, vol. 4, pp. 55–60, 2005.

[21] E. A. Levine, R. I. Freimanis, N. D. Perrier et al., "Positron emission mammography: initial clinical results," *Annals of Surgical Oncology*, vol. 10, pp. 86–91, 2003.

[22] E. L. Rosen, T. G. Turkington, M. S. Soo, J. A. Baker, and R. E. Coleman, "Detection of primary breast carcinoma with a dedicated, large-field-of-view FDG PET mammography device: Initial experience," *Radiology*, vol. 234, no. 2, pp. 527–534, 2005.

[23] L. Tafra, Z. Cheng, J. Uddo et al., "Pilot clinical trial of FDG positron emission mammography in the surgical management of breast cancer," *Annals of Surgical Oncology*, vol. 190, pp. 628–632, 2005.

[24] A. Aliaga, J. A. Rousseau, R. Ouellette et al., "Breast cancer models to study the expression of estrogen receptors with small animal PET imaging," *Nuclear Medicine and Biology*, vol. 31, no. 6, pp. 761–770, 2004.

[25] C. Caldarella, G. Treglia, and A. Giordano, "Diagnostic performance of dedicated positron emission mammography using fluorine-18-fluorodeoxyglucose in women with suspicious breast lesions: A meta-analysis," *Clinical Breast Cancer*, vol. 14, no. 4, pp. 241–248, 2014.

[26] Y. Yamamoto, Y. Ozawa, K. Kubouchi, S. Nakamura, Y. Nakajima, and T. Inoue, "Comparative analysis of imaging sensitivity of positron emission mammography and whole-body PET in relation to tumor size," *Clinical Nuclear Medicine*, vol. 40, no. 1, pp. 21–25, 2015.

[27] L. Li, X.-Y. Gu, D.-W. Li et al., "Performance evaluation and initial clinical test of the positron emission mammography system (PEMi)," *IEEE Transactions on Nuclear Science*, vol. 62, no. 5, pp. 2048–2056, 2015.

[28] K. Schilling, D. Narayanan, J. E. Kalinyak et al., "Positron emission mammography in breast cancer presurgical planning: Comparisons with magnetic resonance imaging," *European Journal of Nuclear Medicine and Molecular Imaging*, vol. 38, no. 1, pp. 23–36, 2011.

[29] J. E. Kalinyak, W. A. Berg, K. Schilling et al., "Breast cancer detection using high-resolution breast WBPET compared to whole-body WBPET or WBPET/CT," *The European Journal of Nuclear Medicine and Molecular Imaging*, vol. 41, pp. 260–275, 2014.

[30] R. L. Wahl, "Current status of PET in breast cancer imaging, staging, and therapy," *Seminars in Roentgenology*, vol. 36, no. 3, pp. 250–260, 2001.

[31] A. Mavi, M. Urhan, Y. u. JQ et al., "Dual time point 18F-FDG WBPET imaging detects breast cancer with high sensitivity and correlates well with histologic subtypes," *Journal of Nuclear Medicine*, vol. 47, pp. 1440–1446, 2006.